

# Assessing the Influence of Sea Surface Temperature and Arctic Sea Ice Cover on the Uncertainty in the Northern Winter Future Climate Projections

Ho Nam Cheung (✉ [zhanghlan5@mail.sysu.edu.cn](mailto:zhanghlan5@mail.sysu.edu.cn))

Sun Yet-sen University

Noel Keenlyside

University of Bergen: Universitetet i Bergen

Torben Koenigk

Swedish Meteorological and Hydrological Institute: Sveriges meteorologiska och hydrologiska institut

Shuting Yang

Danish Meteorological Institute: Danmarks Meteorologiske Institut

Tian Tian

Danish Meteorological Institute: Danmarks Meteorologiske Institut

Zhiqing Xu

CAS Institute of Atmospheric Physics: Institute of Atmospheric Physics Chinese Academy of Sciences

Yongqi Gao

Nansen Environmental and Remote Sensing Center

Fumiaki Ogawa

Hokkaido University: Hokkaido Daigaku

Nour-Eddine Omrani

University of Bergen: Universitetet i Bergen

Shaobo Qiao

Sun Yat-Sen University

Wen Zhou

City University of Hong Kong

---

## Research Article

**Keywords:** climate change, uncertainty in climate projections, winter climate, Aleutian low, Icelandic low

**Posted Date:** April 20th, 2021

**DOI:** <https://doi.org/10.21203/rs.3.rs-375345/v1>

**License:** © ⓘ This work is licensed under a Creative Commons Attribution 4.0 International License.

[Read Full License](#)

---

# Assessing the Influence of Sea Surface Temperature and Arctic Sea Ice Cover on the Uncertainty in the Northern Winter Future Climate Projections

Ho-Nam Cheung<sup>1,2#</sup>, Noel Keenlyside<sup>3,4,5</sup>, Torben Koenigk<sup>6,7</sup>, Shuting Yang<sup>8</sup>, Tian Tian<sup>8</sup>, Zhiqing Xu<sup>9</sup>, Yongqi Gao<sup>5,9</sup>, Fumiaki Ogawa<sup>10</sup>, Nour-Eddine Omrani<sup>3,4</sup>, Shaobo Qiao<sup>1,2</sup>, Wen Zhou<sup>11,12</sup>

1. *School of Atmospheric Sciences & Guangdong Province Key Laboratory for Climate Change and Natural Disaster Studies, Sun Yat-sen University, Zhuhai, China*
2. *Southern Marine Science and Engineering Guangdong Laboratory (Zhuhai), Zhuhai, China*
3. *Geophysical Institute, University of Bergen, Bergen, Norway*
4. *Bjerknes Centre for Climate Research, University of Bergen, Bergen, Norway*
5. *Nansen Environmental and Remote Sensing Center, Bergen, Norway*
6. *Swedish Meteorological and Hydrological Institute, Norrköping, Sweden*
7. *Bolin Centre for Climate Research, Stockholm University, Stockholm, Sweden*
8. *Danish Meteorological Institute, Copenhagen, Denmark*
9. *Nansen-Zhu International Research Centre, Institute of Atmospheric Physics, Chinese Academy of Sciences, Beijing, China*
10. *Graduate School of Science, Hokkaido University, Japan*
11. *Guy Carpenter Asia-Pacific Climate Impact Centre, School of Energy and Environment, City University of Hong Kong, Hong Kong, China*
12. *Center for Ocean Research in Hong Kong and Macau (CORE), School of Energy and Environment, City University of Hong Kong, Hong Kong, China*

Submitted to *Climate Dynamics*

March 2021

# Corresponding author: Ho-Nam Cheung. Email: zhanghlan5@mail.sysu.edu.cn.

## Abstract

1  
2 We investigate the uncertainty (i.e., inter-model spread) in future projections of the northern  
3 winter climate, based on the forced response in the CMIP5 RCP8.5 scenario. The uncertainty  
4 in the forced response of sea level pressure (SLP) is large in the North Pacific, the North  
5 Atlantic, and the Arctic. A major part of these uncertainties (31%) is marked by a pattern with  
6 a center in the northeastern Pacific and a dipole over the northeastern Atlantic that we label as  
7 the Pacific–Atlantic SLP uncertainty pattern ( $PA_{\Delta SLP}$ ). To better understand the nature of  
8  $PA_{\Delta SLP}$ , the associated sea surface temperature (SST) and Arctic sea ice cover (SIC)  
9 perturbation patterns are prescribed in experiments with two atmospheric models (AGCMs):  
10 CAM4 and IFS.

11 The AGCM experiments indicate more robust SLP response over the North Pacific driven  
12 by the SST perturbation, which is associated with the tropical-midlatitude interaction and the  
13 Rossby wavetrain. The North Atlantic SLP response is better explained by the joint effect of  
14 SST and SIC perturbations, which is partly related to the Rossby wavetrain from the Pacific  
15 and the air–sea interactions over the North Atlantic. However, these responses shift westward  
16 relative to  $PA_{\Delta SLP}$ , where in CAM4 it is related to the low-frequency transient eddy forcing.  
17 The magnitude of these responses in the two AGCMs is largely different. Thus, constraining  
18 only the SST and SIC projections might not alone help constrain future climate projections. We  
19 should investigate the role of other factors in these uncertainties, such as the atmosphere–SST–  
20 SIC coupled dynamics.

21 **Keywords:** climate change, uncertainty in climate projections, winter climate, Aleutian low,  
22 Icelandic low

## 23 **1. Introduction**

24 There is great concern on if and how the intensity and location of large-scale near-surface  
25 circulation features (e.g., sea level pressure, SLP, near the Aleutian low and the Icelandic low)  
26 and their associated high-impact weather will change with global warming. Climate models  
27 consistently simulate a significant and systematic increase in surface air temperature in the high  
28 emission scenarios. Still, they show a large discrepancy in the magnitude of global warming  
29 because of their different climate sensitivity (Andrew et al. 2012; Vial et al. 2013; Hu et al.  
30 2017, 2020). The magnitude of warming also shows discrepancies with latitude and altitude  
31 that are associated with differences in the hemispheric temperature gradient and the large-scale  
32 atmospheric circulation features. In particular, there is a large disagreement in terms of the  
33 magnitude and sign in future projections of midlatitude atmospheric circulation for the end of  
34 this century, even when considering only the dominant external forcing (Shepherd 2014;  
35 Cheung et al. 2018). To better interpret and constraint future climate projections, we need to  
36 better understand the dynamics underlying the uncertainty in future projections of large-scale  
37 atmospheric circulation.

38 Tropical upper-tropospheric warming and Arctic lower tropospheric warming (also called  
39 Arctic amplification) are two prominent temperature responses to global warming. Specifically,  
40 climate models consistently simulate stronger tropical warming in the upper troposphere. This  
41 accompanies an increase in the upper-tropospheric equator-to-pole temperature gradient. This  
42 would cause an increase in the midlatitude zonal wind speed, and a poleward shift in the jet  
43 stream and storm tracks (Yin 2005; Chang et al., 2012; Barnes and Polvani 2013). On the other  
44 hand, the models robustly simulate stronger Arctic warming in the lower troposphere. This  
45 accompanies a decrease in the equator-to-pole temperature gradient. This would cause a  
46 reduction in the midlatitude zonal wind speed, and an equatorward shift in the jet stream due to

47 the thermal wind balance (Harvey et al. 2015). In CMIP3 and CMIP5 models, the uncertainty  
48 in future projections of jet stream and storm tracks is partly related to these competing effects  
49 (Barnes and Screen 2015; Shaw et al. 2016). While the model-mean global warming response  
50 tends to be a poleward shift of the jet stream, the inter-model spread in the projected change in  
51 zonal wind speed is linked to the spread in Arctic amplification, tropical warming, and the  
52 strength of stratospheric polar vortex (Manzini et al. 2014; Barnes and Screen 2015; Zappa and  
53 Shepherd 2017; Cheung et al. 2018; Oudar et al. 2020). In particular, a stronger Arctic  
54 amplification tends to be associated with a weaker and southward shift of the jet stream; this is  
55 opposite in sign to the mean change (Deser et al. 2015; Yim et al. 2016).

56 Previous studies have related the uncertainty in future projections of regional atmospheric  
57 circulation to the uncertainty in future projections of sea surface temperature (SST) and Arctic  
58 sea ice cover (SIC). Over the North Pacific, climate models tend to project a deeper and a  
59 northward expansion of the Aleutian low in the future (Gan et al. 2017; see also Fig. 1a).  
60 However, future projections of the southeastern and northwestern parts of the Aleutian low have  
61 a large uncertainty that is strongly linked to the zonal SST gradient in the equatorial Pacific (an  
62 El Niño-like mean state; Gan et al. 2017). Besides the El Niño-like signal, the uncertainty in  
63 future projections of the Aleutian low is related to the land-sea thermal contrast between the  
64 Asian continent and the Pacific Ocean, and the associated zonal pressure gradient between the  
65 Siberian high and the Aleutian low (Gan et al. 2017). Choi et al. (2016) found that the  
66 uncertainty in future projections of SLP over the eastern North Pacific is related to a Pacific  
67 Decadal Oscillation (PDO)-like SST signal, where the SST anomalies are strongest in the  
68 midlatitudes.

69 Over the North Atlantic, the multi-model mean (MME) of future climate projections  
70 indicates a slight positive trend of the wintertime North Atlantic Oscillation (NAO) and a

71 northeastward extension of the storm tracks (Bader et al. 2011; Woollings et al. 2012; Lau and  
72 Ploshay 2013), but these projections have a large uncertainty. Some studies suggest that this  
73 uncertainty is driven by remote forcing (Harvey et al. 2015; Ciasto et al. 2016), with relatively  
74 little impact from local SST in these models (Hand et al. (2019), whereas some studies suggest  
75 local SST contribute to the uncertainty (Gervais et al. 2019). On one hand, the uncertainty in  
76 the future projections of Arctic SIC causes that of lower tropospheric equator-to-pole  
77 temperature gradient and the North Atlantic storm tracks (Harvey et al. 2015). The decline in  
78 Arctic SIC also favors a negative NAO-like response and a higher SLP response over the  
79 northern Eurasia (Peings and Magnsdottir 2014; Deser et al. 2016; Blackport and Kushner 2017;  
80 Zappa et al. 2018). On the other hand, the uncertainty in future projections of tropical Pacific  
81 SST may affect the midlatitude teleconnections, through exciting the Pacific–North America  
82 pattern. This is strongly linked to the uncertainty in future projections of the jet streams over  
83 the North Pacific and the North Atlantic (Delcambre et al. 2013), the North Atlantic storm  
84 tracks (Ciasto et al. 2016), and the northern annual mode (Cattiaux and Cassou 2013).

85 Based on aforementioned studies, we hypothesize that the uncertainty in future projections  
86 of SST and SIC could cause that of the Northern Hemisphere atmospheric circulation. Although  
87 previous studies have analyzed the relative contribution of SST and SIC to this uncertainty, few  
88 studies have used more than one model to assess the robustness of these linkages and to  
89 understand the underlying mechanisms. To address this issue, we perform experiments with  
90 two atmosphere-only general circulation models (AGCMs) using the monthly-varying SST and  
91 SIC patterns that are related to the uncertainty in future projections of the SLP. We will deduce  
92 if future climate projections of the SLP could be constrained by improving the simulations of  
93 specific SST and SIC patterns. Specifically, we address the following questions:

- 94 1) What are the large-scale spatial patterns representing the uncertainty in future projections  
95 of the Northern Hemisphere SLP? What are the corresponding SST and SIC patterns?  
96 2) To what extent do AGCMs reproduce these SLP patterns when forced by these  
97 corresponding SST and SIC patterns? Do the mechanisms simulated by the AGCMs  
98 correspond to those of the CMIP5 inter-model differences, estimated from ten models  
99 with at least three ensemble members?

100 We focus on the winter (DJF) climate projections from the CMIP5 RCP8.5 scenario, which  
101 is the highest emission scenario and thus produces the strongest externally forced responses.  
102 The projected climate change is considered for the late twenty-first century (2069/70–2098/99)  
103 relative to the late twentieth century (1971/72–2000/01), which is referred to as “response”  
104 hereafter. For example, the projected change of SLP is called the SLP response.

105 To identify uncertainties that are inherent to individual models requires large-ensemble  
106 simulations (Deser et al. 2020). This is especially true for the extratropical circulation where  
107 large internal climate variability can even mask the signals from strong external forcing (Deser  
108 et al. 2012). Thus, we analyze simulations from ten CMIP5 coupled models that have *at least*  
109 *three ensemble members* in the historical and RCP8.5 runs (Table 1); this is to try to minimally  
110 limit noise from internal variability. This selection was limited by the availability of model  
111 simulations at the time this study was started. (CSIRO-Mk-3.6.0 was also available, but is not  
112 included because its SST and SIC biases were too large). We average across ensemble members  
113 of each model to increase the signal-to-noise ratio for the external forcing, where the response  
114 averaged across the ensemble members is called the “forced response”. The MME forced  
115 response is the unweighted average of the forced response from the ten CMIP5 models.

116 Section 2 presents analysis of the uncertainty in the forced response of DJF SLP from the  
117 ten CMIP5 models. Section 3 describes the design of sensitivity experiments. Section 4

118 compares simulated responses from the sensitivity experiments to the uncertainty in forced  
119 responses of the ten CMIP5 models, and analyzes the possible dynamics. Section 5 provides a  
120 discussion and conclusion.

## 121 **2. Uncertainty in the forced response of DJF SLP**

122 The ten CMIP5 models consistently indicate that global warming will cause SLP to decrease  
123 in the high-latitudes over the Arctic, Northeast America, and North Pacific (Fig. 1a).  
124 Concomitantly, SLP increases over the midlatitude North Atlantic near the Icelandic low and  
125 the Mediterranean (Fig. 1a). These results are generally consistent with Collins et al. (2013;  
126 their Fig. 12.18), except that weakening of the Icelandic low is substantial in the ten CMIP5  
127 models. In contrast, these models do not agree well on the forced SLP response in the  
128 subtropical region ( $\sim 30^\circ\text{--}40^\circ\text{N}$ ), including the Azores high, the eastern North Pacific, the  
129 Middle East and the East Asian continent (i.e., as there is little agreement on sign of the response,  
130 as indicated by the absences of dots). The agreement is also small in the northeastern flank of  
131 the Icelandic low and Scandinavia, as well as the southeastern part of the Aleutian low.

132 The uncertainty in the forced SLP response is quantified by the inter-model standard  
133 deviation (computed from the individual model ensemble means; Fig. 1b). The uncertainty is  
134 largest near the center of Aleutian low, and is large over the Canadian Archipelago and the  
135 northeastern Atlantic (east of the Icelandic low). Compared to the uncertainty in the forced SLP  
136 response (Fig. 1b), the internal climate variability<sup>1</sup> in the SLP response is significantly higher  
137 over the Eurasian side of the Arctic and it is comparable over the northeastern Atlantic and the  
138 high-latitude Eurasia (Fig. 1c). This highlights the importance of using more than three  
139 ensemble members to reduce the internal climate variability. The internal climate variability in

---

<sup>1</sup> Internal climate variability is estimated by the intra-model standard deviation, where the standard deviation computed from the individual ensemble members removing the ensemble mean of each model.

140 the ensemble mean is reduced by one over the square root of the ensemble size, and for the  
141 three members is  $\sim 0.6$ . The selected ten CMIP5 models appear to largely capture the uncertainty  
142 and internal variability in the response across the 34 available CMIP5 models: the uncertainty  
143 pattern computed from all ensemble members of the ten CMIP5 models is very similar to that  
144 computed from single ensemble members of the 34 available CMIP5 models (pattern  
145 correlation of +0.94), with only slightly lower amplitude (Fig. S1). It should be stressed that the  
146 inter-model spread of the 34 CMIP5 models does not provide a good estimate of the uncertainty  
147 in the forced response over the northeastern Atlantic and high latitudes, where the internal  
148 variability is large.

149 The dominant modes of the uncertainty in the forced SLP response are identified by  
150 performing an inter-model empirical orthogonal function (EOF) analysis on the forced response  
151 in DJF SLP from the ten CMIP5 models over the domain  $20^{\circ}$ – $90^{\circ}$ N (Fig. 2). In the EOF analysis,  
152 the MME forced response is removed prior to computing the covariance matrix, which is  
153 weighted by the square root of the cosine of latitude to account for the change in grid size. As  
154 shown in Fig. 2a, the first mode (EOF1) has the strongest positive loading over the North Pacific  
155 and mainly characterizes weakening or strengthening of the Aleutian low, but also has a positive  
156 loading over the northeastern Atlantic and a negative loading near the Mediterranean. The  
157 second mode (EOF2) has a strong positive loading over the southeastern flank of the Icelandic  
158 low and a strong negative loading over the Hudson Bay ( $60^{\circ}$ N,  $90^{\circ}$ W; Fig. 2b). The spatial  
159 pattern of EOF2 over the North Pacific represents a shift in the Aleutian low, with a positive  
160 loading in its eastern flank and a negative loading in its northwestern flank. Overall, EOF1 and  
161 EOF2 separately capture the two major centers in the uncertainty in the forced SLP response  
162 (Fig. 1b).

163 Previous studies have investigated the uncertainty in circulation responses over the North  
164 Pacific (e.g., Gan et al. 2017) and the North Atlantic (e.g., Harvey et al. 2015) separately.  
165 However, the uncertainty in the forced SLP response over the northeastern Pacific ( $40^{\circ}$ – $65^{\circ}$ N  
166 and  $160^{\circ}$ – $135^{\circ}$ W) and over the northeastern Atlantic ( $60^{\circ}$ – $85^{\circ}$ N and  $20^{\circ}$ W– $10^{\circ}$ E) is strongly  
167 correlated ( $+0.770$ ,  $p < 0.05$ , Fig. 2d). These uncertainties are partly captured by EOF1 and  
168 EOF2, which are not well separated according to the North’s rule of thumb (North et al. 1982).  
169 In other words, the EOF analysis is not able to isolate the coherence of the SLP response over  
170 the Pacific and the Atlantic in the ten CMIP5 models. Thus, we adopt a simple approach to  
171 adequately represent this coherence: we add EOF1 and EOF2 to form a Pacific–Atlantic SLP  
172 uncertainty pattern ( $PA_{\Delta SLP}$ )<sup>2</sup> that captures both uncertainties (Fig. 2c) and accounts for 31% of  
173 the total variance. The forced SLP response in the ten CMIP5 models is projected onto the  
174  $PA_{\Delta SLP}$  pattern to get an index ( $PAI_{\Delta SLP} = PC1 + PC2$ ) for the SLP uncertainty among the models.

### 175 **3. Methods**

#### 176 **3.1 Models**

177 We use two atmosphere general circulation models (AGCMs) in order to understand the  
178 impact of SST and Arctic sea ice on the uncertainty in the forced SLP response. The first AGCM  
179 is version 4.0 of the Community Atmosphere Model (CAM4) developed by the National Center  
180 for Atmospheric Research (NCAR) with a horizontal resolution of  $0.9^{\circ} \times 1.25^{\circ}$  (~100 km) and  
181 26 vertical levels up to 3 hPa (Neale et al. 2013). The second AGCM is the atmospheric  
182 component of the EC-Earth 3.1 model (Hazeleger et al. 2010), which is based on the Integrated  
183 Forecast System (IFS) cycle 36r4 developed by the European Centre for Medium-Range

---

<sup>2</sup> This operation describes a 45-degree rotation in EOF1-EOF2 space. We add EOF1 and EOF2 because (i) the SLP uncertainty over the northeastern Pacific and over the northeastern Atlantic is significantly positively correlated, and (ii) in both EOF1 and EOF2 these two regions are of the same sign.

184 Weather Forecasts (ECMWF). Here, IFS is used in T255 horizontal resolution (~80 km) with  
185 91 vertical levels up to 0.01 hPa (Balsamo et al. 2009).

## 186 **3.2 Design of experiments**

### 187 3.2.1 Prescribed SST and SIC patterns

188 In the experiments, we prescribe SST and SIC patterns ( $SST_{\Delta SLP}$  and  $SIC_{\Delta SLP}$ ) that are  
189 computed by linear regression of the forced response in SST and SIC against  $PAI_{\Delta SLP}$  across  
190 the ten CMIP5 models; the patterns are computed for each calendar month and have an  
191 amplitude that corresponds to one unit of the standardized index. To attribute a physical  
192 meaning of SST and SIC patterns, we illustrate the inter-model regression patterns of DJF SST  
193 and SIC; these are referred to as the DJF  $SST_{\Delta SLP}$  and  $SIC_{\Delta SLP}$  (Fig. 3a–b). Note that  $SST_{\Delta SLP}$   
194 is global and  $SIC_{\Delta SLP}$  is restricted to the Northern Hemisphere.

195 The uncertainty in the forced SST response is generally larger at high latitudes (Fig. 3a). In  
196 the Northern Hemisphere, it is especially large over the Barents-Kara Sea and the midlatitude  
197 North Atlantic. The DJF  $SST_{\Delta SLP}$  (associated with positive  $PAI_{\Delta SLP}$ ) captures these SST  
198 uncertainties, representing a substantial weakening in the MME forced response of the SST  
199 gradient between the tropics and the northern high-latitudes (Fig. 3c).  $SST_{\Delta SLP}$  also represents  
200 a warmer Northern Hemisphere and a cooler Southern Hemisphere than the MME climate  
201 response, suggesting that  $PAI_{\Delta SLP}$  also co-varies with a reduced inter-hemispheric SST gradient  
202 (Fig. 3d). Moreover,  $SST_{\Delta SLP}$  is associated with weakening in the zonal SST gradient between  
203 the equatorial western and eastern Pacific, where the climatological mean SST is higher in the  
204 western Pacific (warm-pool region).

205 The uncertainty in the forced response of the Arctic SIC is largest in the Kara Sea (~60°–  
206 90°E) and has a secondary maximum north of the Laptev Sea (~120°E) (Fig. 3b). The DJF

207 SIC<sub>ASLP</sub> represents a decline in the entire Arctic with a larger decline in these two seas.  
208 Therefore, PA<sub>ASLP</sub> co-varies with the total Arctic sea ice extent (Fig. 3e) in a consistent manner  
209 with the high-latitude SST (Fig. 3a).

### 210 3.2.2 “Time-slice” sensitivity experiments

211 We conducted three sets of AGCM “time-slice” sensitivity experiments forced by monthly-  
212 varying SST and SIC repeated for 60 annual cycles in CAM4 and 50 annual cycles in IFS (Table  
213 2), such that the mean response in each model largely increases the signal-to-noise ratio. The  
214 prescribed SST and SIC are based on the 2069–2098 monthly climatology in the CMIP5  
215 RCP8.5 scenario (SST<sub>MME</sub> and SIC<sub>MME</sub>) and the monthly-varying SST<sub>ASLP</sub> and SIC<sub>ASLP</sub> (Section  
216 3a; Fig. S2 and Fig. S3). Consistently, the prescribed radiative forcing (greenhouse gas  
217 concentrations and aerosol concentrations) are the 2069–2098 monthly climatology from the  
218 CMIP5 RCP8.5 scenario.

219 When the boundary conditions of SST and SIC in any set of sensitivity experiments were  
220 modified, half the monthly-varying SST<sub>ASLP</sub> and SIC<sub>ASLP</sub> was added or subtracted. The  
221 difference between the boundary conditions of two runs in one set of experiments is equivalent  
222 to one unit of the inter-model regression patterns of SST and SIC. Thus, the magnitude of  
223 atmospheric response can be directly compared to that of the inter-model regression pattern  
224 from the ten CMIP5 models.

225 In the first set of experiments (run1 and run2), both SST and SIC were modified and they  
226 are called SST+SIC perturbation runs. In run1, half the monthly-varying SST<sub>ASLP</sub> and SIC<sub>ASLP</sub>  
227 was added to the 2069–2098 monthly climatology of SST and SIC respectively (SST<sub>MME</sub> and  
228 SIC<sub>MME</sub>) to form the boundary conditions. Conversely, in run2, half the monthly-varying  
229 SST<sub>ASLP</sub> and SIC<sub>ASLP</sub> was subtracted from SST<sub>MME</sub> and SIC<sub>MME</sub> to form the boundary conditions.  
230 It is assumed that SST and SIC change coherently as the inter-model regression analysis (Fig.

231 S2 and Fig. S3), so we did not perform experiments with the boundary conditions  
232  $SST_{MME}+SST_{\Delta SLP}$  with  $SIC_{MME}-SIC_{\Delta SLP}$ , and  $SST_{MME}-SST_{\Delta SLP}$  with  $SIC_{MME}+SIC_{\Delta SLP}$ . In the  
233 second set of experiments (run3 and run4), SST was changed as in run1 and run2 while SIC  
234 was the  $SIC_{MME}$ ; they are called SST perturbation runs. In the third set of experiments (run5  
235 and run6), SIC was changed as in run1 and run2 while SST was the  $SST_{MME}$ ; they are called  
236 SIC perturbation runs.

237 We follow Screen et al. (2013)'s approach to ensure that SST and SIC are consistent with  
238 each other in the second and third sets of experiments (runs 3–6). In particular, for grid cells  
239 with sizeable SIC perturbation ( $|SIC_{\Delta SLP}| \geq +0.1$  (fraction)), the boundary condition of SST was  
240 modified to  $SST_{MME}$  in the SST perturbation runs (run3 and run4) and to  $SST_{MME} \pm 0.5 \times SST_{\Delta SLP}$   
241 in the SIC perturbation runs (run5 and run6). Otherwise the boundary condition of SST was set  
242 as in Table 2. The monthly-varying SIC boundary condition of run 1 and run 5 (larger SIC and  
243 SST response) and the monthly-varying SIC boundary condition of run 2 and run 6 (smaller  
244 SIC and SST response) are shown in Fig. S4 and Fig. S5, respectively.

### 245 3.3 Diagnostics

246 Because the SST perturbation represents a weaker meridional SST gradient between the  
247 low and high latitudes and the SIC perturbation represents a stronger decline of pan-Arctic SIC,  
248 we investigate if the response in the zonal-mean streamfunction is related to the SST and SIC  
249 perturbations. Moreover, circulation anomalies are often linked with a midlatitude Rossby  
250 wavetrain (teleconnection) excited by tropical SST forcing (Horel and Wallace 1981; Ding et  
251 al. 2014). To link the tropical circulation to the midlatitude atmospheric circulation, we will  
252 present responses in the divergent wind  $V_z$ , the velocity potential ( $\chi = \nabla^{-2} (\nabla \cdot V)$ ) and the  
253 Rossby wave source (S), where the Rossby wave source is defined as in Sardeshmukh and  
254 Hoskins (1988):

$$255 \quad S' = \underbrace{-\bar{\zeta} \nabla \cdot V'_{\chi} - \zeta' \nabla \cdot \bar{V}_{\chi}}_{\text{stretching}} \underbrace{-\bar{V}_{\chi} \cdot \nabla \zeta' - V'_{\chi} \cdot \nabla \bar{\zeta}}_{\text{advection}} \quad (1)$$

256 where  $\zeta$  is the absolute vorticity. The overbar denotes the basic state and the prime denotes the  
 257 inter-model regression of the forced response against  $\text{PAI}_{\Delta\text{SLP}}$  across the ten CMIP5 models or  
 258 the response in the AGCM sensitivity experiments. On the R.H.S. of (1), the first two terms are  
 259 the contribution from the vortex stretching, where in the first (second) term a stronger  
 260 convergence of the wind response (climatology) would enhance the cyclonic Rossby wave  
 261 source, while stronger divergence would enhance the anticyclonic Rossby wave source. The  
 262 third and fourth terms are the contribution from the vorticity advection by the divergent wind,  
 263 where the region with a strong vorticity gradient would enhance or reduce the Rossby wave  
 264 source. When the response of Rossby wave source is compared to the pressure response, we  
 265 could deduce if the tropical–midlatitude interaction is crucial for the pressure response.

266 To further demonstrate if the midlatitude atmospheric response is a Rossby wave train, we  
 267 will present the horizontal component of stationary wave activity fluxes at the 250-hPa (Takaya  
 268 and Nakamura 2001):

$$269 \quad \mathbf{W} = \frac{p \cos \phi}{2|V|} \left\{ \begin{array}{l} \frac{U}{a^2 \cos^2 \phi} \left[ \left( \frac{\partial \psi'}{\partial \lambda} \right)^2 - \psi' \frac{\partial^2 \psi'}{\partial \lambda^2} \right] + \frac{V}{a^2 \cos \phi} \left( \frac{\partial \psi'}{\partial \lambda} \frac{\partial \psi'}{\partial \phi} - \psi' \frac{\partial^2 \psi'}{\partial \lambda \partial \phi} \right) \\ \frac{U}{a^2 \cos^2 \phi} \left( \frac{\partial \psi'}{\partial \lambda} \frac{\partial \psi'}{\partial \phi} - \psi' \frac{\partial^2 \psi'}{\partial \lambda \partial \phi} \right) + \frac{V}{a^2} \left[ \left( \frac{\partial \psi'}{\partial \phi} \right)^2 - \psi' \frac{\partial^2 \psi'}{\partial \phi^2} \right] \end{array} \right\} \quad (2)$$

270 where  $U$  and  $V$  are the zonal and meridional component of the basic flow  $\mathbf{V}$ ,  $p$  is the pressure  
 271 level,  $\psi'$  is the inter-model regression of the forced response against  $\text{I}_{\Delta\text{SLP}}$  across the ten CMIP5  
 272 models or the streamfunction response in the AGCM sensitivity experiments. Because the  
 273 direction of wave activity fluxes is parallel to the group velocity, this diagnostic identifies the  
 274 response in Rossby wave propagation.

## 275 **4. Results**

### 276 **4.1 Mechanisms underlying the CMIP5 SLP uncertainty pattern**

277 We now identify the potential mechanisms explaining the relation between the SLP  
278 uncertainty pattern ( $PA_{\Delta SLP}$ ) and the SST and SIC uncertainty patterns in the ten CMIP5 models.  
279 The regression of  $PAI_{\Delta SLP}$  against the forced DJF SLP response reveals increasing SLP in the  
280 northeastern Pacific and the northeastern Atlantic (Fig. 4a). These positive SLP regions  
281 coincide with positive 250-hPa height regions (Fig. 4b), suggesting an equivalent barotropic  
282 high structure. Moreover, positive  $PAI_{\Delta SLP}$  is associated with increasing SLP over the tropical  
283 Indo-Pacific and decreasing SLP in the sea ice region, including the Arctic and Northeast  
284 America with a maximum around the Canadian Archipelago (Fig. 4a). It is also associated with  
285 a dipole pattern over Eurasia, with increasing SLP near the latitude of the Icelandic low and  
286 decreasing SLP in the Mediterranean and the Middle East (Fig. 4a). We will investigate how  
287 these SLP uncertainties are related to the zonal-mean meridional cells, the air-sea interactions  
288 and the midlatitude Rossby wavetrain.

289 From the zonal-mean perspective,  $SST_{\Delta SLP}$  represents anomalous warming in the Northern  
290 Hemisphere and anomalous cooling in the Southern Hemisphere (Fig. 3d). This SST pattern is  
291 associated with more zonal-mean precipitation in the northern tropics and less zonal-mean  
292 precipitation in the southern tropics, i.e., northward shift of the inter-tropical convergence zone  
293 (ITCZ; Fig. 5a). The northward shift of the ITCZ is associated with 10–20% weakening of the  
294 Hadley circulation except in the upper troposphere (Fig. 5a), where the DJF climatological  
295 Hadley cell represents a circulation from the Southern Hemisphere to the Northern Hemisphere.  
296 The northern hemisphere Ferrel and polar cells also slightly weaken (Fig. 5a). These changes  
297 are consistent with an expected weakened poleward heat transport in the Northern Hemisphere  
298 (Kang et al. 2009; Schneider et al. 2014). Note that  $PAI_{\Delta SLP}$  is weakly correlated to the forced

299 responses in the zonal-mean upper-tropospheric temperature ( $<0.2^{\circ}\text{C}$ ; Fig. S6a) and the global-  
300 mean surface temperature. In other words, the tropical precipitation changes associated with  
301  $\text{PA}_{\Delta\text{SLP}}$  are not driven by the moist convective processes related to global warming. Consistently,  
302 the circulation uncertainties described by  $\text{PA}_{\Delta\text{SLP}}$  are not strongly related to the climate  
303 sensitivity. Hence, it is important to investigate the factors other than the climate sensitivity  
304 contributing to the SLP uncertainties.

305 Regionally,  $\text{SST}_{\Delta\text{SLP}}$  over the tropical region is strongest in the eastern Pacific (Fig. 3a). The  
306 stronger warming over the tropical eastern Pacific accompanies stronger local convection and  
307 precipitation ( $\sim 10^{\circ}\text{--}15^{\circ}\text{N}$  and  $150^{\circ}\text{--}130^{\circ}\text{W}$ ; Fig. 6a). These accompany lower velocity  
308 potential and stronger divergent wind at the 250 hPa blowing northeastwards from the tropical  
309 region to the midlatitudes in the eastern North Pacific (Fig. 6b). The convergent wind is  
310 associated with a cyclonic (i.e., positive sign) Rossby wave source (Fig. 6c). Meanwhile, the  
311 region with a large gradient in the velocity potential is associated with an anticyclonic (i.e.,  
312 negative sign) Rossby wave source and an anomalous anticyclone over the central North Pacific.  
313 The anticyclonic Rossby wave source accompanies the emanation of a Rossby wavetrain from  
314 the anomalous anticyclone. This wavetrain propagates eastward to an anomalous cyclone over  
315 the North American west coast and then propagates southeastward to the Gulf of Mexico (Fig.  
316 6c). It appears that the tropical–midlatitude interactions over the Pacific is essential for the  
317 northeastern Pacific SLP uncertainty. Moreover, because the wavetrain does not propagate  
318 further from North America to the northeastern Atlantic, the local air-sea interaction appears to  
319 be important in the northeastern Atlantic SLP uncertainty.

## 320 **4.2 Atmospheric impact of the SST+SIC uncertainty patterns**

321 Next we use AGCM experiments to assess the extent to which the SST and SIC drive  $\text{PA}_{\Delta\text{SLP}}$   
322 and whether the mechanisms identified above hold. The SLP response of CAM4 in the

323 SST+SIC perturbation runs has a positive center over the midlatitude North Pacific and a dipole  
324 pattern over the North Atlantic (Fig. 4c). The pattern has features similar to the CMIP5 inter-  
325 model regression although the positive and negative centers shift westward (Fig. 4c vs. Fig. 4a);  
326 the possible reason causing the westward shift will be studied later in this section. The pattern  
327 correlation between the CAM4 SLP response and the SLP inter-model regression pattern from  
328 the ten CMIP5 models increases from +0.381 to +0.731 when the CAM4 SLP response is  
329 shifted zonally by 35°. The CAM4 simulations also shows good correspondence between the  
330 SLP pattern and the 250-hPa height pattern (Fig. 4c,d). On the other hand, the SLP and 250-  
331 hPa height response of IFS is generally weaker than CAM4, with a positive response over the  
332 North Pacific and a dipole-like structure over the North Atlantic (Fig. 4e,f). In short, CAM4  
333 and IFS tend to simulate coherent atmospheric responses over the oceans. Comparatively, the  
334 CAM4 response is closer to the inter-model regression from the ten CMIP5 models, and the  
335 IFS response is weaker, especially over the North Pacific

336 The zonal-mean response of the two AGCMs shows suppressed precipitation in the southern  
337 tropics and enhanced precipitation in the northern tropics, and the ITCZ shifts towards the  
338 northern tropics (Fig. 5b,c). These precipitation responses are unlikely driven by the moist  
339 convective processes because the response in upper-tropospheric warming is weak (Fig. S6b,c).  
340 Moreover, the two AGCMs robustly simulate substantial weakening in the Hadley cell between  
341 10°S and 10°N (Fig. 5b,c), which accompanies weaker poleward heat transport in the Northern  
342 Hemisphere (Kang et al. 2009; Schneider et al. 2014). The tropical zonal-mean circulation  
343 responses of the two AGCMs are generally consistent with the inter-model regression from the  
344 ten CMIP5 models. In mid- and high-latitudes, CAM4 simulates a weak response in Ferrel and  
345 Polar cells, where the southern (northern) edge of the Ferrel cell is enhanced (weakened) (Fig.  
346 5b). On the other hand, IFS simulates more substantial weakening in Ferrel and polar cells (Fig.

347 5c). The center of these responses is located at 45°N and 65°N respectively (Fig. 5c), which  
348 coincides with the two centers of the dipole-like response in the Atlantic (Fig. 4e,f). Therefore,  
349 IFS has a stronger response in the zonal-mean circulation than CAM4 and what is found in the  
350 CMIP5 inter-model difference.

351 Regionally, in CAM4, the Rossby wavetrain response from the North Pacific to the North  
352 Atlantic (Fig. 7e) is associated with strong tropical–midlatitude interaction over the North  
353 Pacific (Fig. 7c), which is related to the enhanced tropical rainfall over the tropical eastern  
354 Pacific (Fig. 7a). The wave activity fluxes propagate northeastward from the North Pacific to  
355 North America and then the propagation turns eastward to the high-latitude North Atlantic (Fig.  
356 7e). The Rossby wavetrain response emanates from the regions with an anticyclonic Rossby  
357 wave source at 30°–40°N over the northwestern Pacific and at 15°N over the northeastern  
358 Pacific, which are due to a larger gradient in the velocity potential (Fig. 7c). Compared to the  
359 inter-model regression from the ten CMIP5 models, the Rossby wavetrain response in CAM4  
360 shifts westward (Fig. 7e vs. Fig. 6c). Although the significant rainfall response in CAM4 is  
361 extended westward from ~155°W to 180° (Fig. 7a vs. Fig. 6a), the associated divergent wind  
362 response over the tropical Pacific is not shifted westward (Fig. 7c vs. Fig. 6b). The westward  
363 extension of the precipitation response cannot explain the westward shift of the Rossby  
364 wavetrain response. Indeed, the midlatitude Northwestern Pacific (where the Rossby wavetrain  
365 emanates) has an easterly wind response, which can be explained by the non-linear forcing by  
366 transient eddies that is not considered in Eq. (1). Specifically, convergence of the low-frequency  
367 (8-day low-pass filtered)  $\mathbf{E}$  vector propagating westward from the northeastern Pacific  
368 corresponds to the easterly wind response (Hoskins et al. 1983; Fig. S7a). The high-frequency  
369 eddy forcing is much weaker than the low-frequency eddy forcing (Fig. S7a,b). The westward  
370 propagating low-frequency  $\mathbf{E}$  vector over the midlatitude North Pacific may explain the

371 westward shift of the geopotential height response and the associated Rossby wavetrain  
372 response. In short, the Rossby wavetrain response in CAM4 is related to the tropical-midlatitude  
373 interactions and the low-frequency transient eddy forcing. Note that the local air-sea interaction  
374 may also be important in the North Atlantic circulation response, because there is limited wave  
375 propagation from the North Pacific to the North Atlantic (Fig. 7e).

376 In IFS, the Rossby wavetrain response over the North Atlantic is separated from the  
377 response over the North Pacific. The Rossby wavetrain response over the North Pacific in IFS  
378 is much weaker than that in CAM4 (Fig. 7f vs. Fig. 7e), which is related to weaker responses  
379 of tropical precipitation and tropical–midlatitude interaction (Fig. 7b,d vs. Fig. 7a,c). The wave  
380 activities fluxes over the North Atlantic are emanated from the region with anticyclonic Rossby  
381 wave source (Fig. 7f). This is associated with enhanced precipitation and stronger divergent  
382 wind at 250-hPa. This appears to be related to strengthening of the local air-sea interactions at  
383 the mid-latitude North Atlantic. The role of transient eddies is not investigated due to the lack  
384 of data availability. The above results suggest that the responses of CAM4 and IFS to the  
385 SST+SIC perturbation have different dynamical mechanisms, where the response of CAM4 is  
386 closer to the CMIP5 inter-model difference.

### 387 **4.3 Separate impact of the SST and SIC uncertainty patterns**

388 The SLP response in the SST+SIC perturbation runs of the AGCMs is not fully consistent  
389 with the forced SLP response from ten CMIP5 models. The CAM4 response has a spatial  
390 pattern similar to the CMIP5 inter-model difference albeit with a zonal shift, whereas the IFS  
391 response is generally weaker than CAM4 and is associated with different dynamic mechanisms.  
392 The difference in the SLP response between the AGCMs and CMIP5 models, as well as the  
393 difference between the two AGCMs, could be contributed by the SST perturbation and/or the  
394 SIC perturbation. Hence, it is instructive to know the influence of the SST and SIC perturbations

395 on the SLP response in the SST+SIC perturbation runs (Figs. 8a–d and 9a–d), and to know  
396 whether the responses to these perturbations are linear (Figs. 8e,f and 9e,f). The impact is  
397 predominantly linear when the SST+SIC response is equal to the sum of the separate responses  
398 of SST and SIC.

399 For CAM4, the linear sum of pressure responses in the SST perturbation runs and the SIC  
400 perturbation runs (shading in Fig. 8e,f) is broadly similar to the pressure responses in the  
401 SST+SIC perturbation runs except those over the Eurasian continent (contour in Fig. 8e,f),  
402 suggesting that the pressure responses of CAM4 in the SST+SIC perturbations can be mainly  
403 linearly explained by their SST and SIC components. Specifically, the pressure responses of  
404 CAM4 in the SST+SIC perturbations are largely explained by the SST perturbation, except for  
405 the region with sea ice (Fig. 8a vs. Fig. 8e). The positive pressure response over the high-latitude  
406 Euro–Atlantic region in the SST+SIC perturbation runs (contour in Fig. 8e,f) is split into two  
407 centers over the Baffin Bay ( $\sim 75^\circ\text{N}$ ,  $70^\circ\text{W}$ ) and the Barents–Kara Sea in the SST perturbation  
408 runs (Fig. 8a,b). The positive pressure response near Greenland (part of the dipole-like response)  
409 is contributed by both SST and SIC perturbations (Fig. 8a,c). The SIC perturbation is the  
410 dominant factor of the Arctic SLP response, and it contributes to the negative SLP response  
411 over the Canadian Archipelago (Fig. 8c). Note that the pressure responses to the SIC  
412 perturbation have smaller signal-to-noise ratios than those responses to the SST perturbation.

413 For IFS, the pressure response pattern in the SST perturbation runs is closer to that in the  
414 SST+SIC perturbation runs than the SIC perturbation runs, but the patterns differ (top panel in  
415 Fig. 9 vs. contour in the bottom panel in Fig. 9). The weak pressure responses over the Arctic  
416 and the North Pacific in the SST+SIC perturbation runs (contour in Fig. 9e,f) are the result of  
417 the opposing effect of the SST perturbation (Fig. 9a,b) and the SIC perturbation (Fig. 9c,d).  
418 However, the linear sum of these pressure responses (shading in Fig. 9e,f) does not resemble

419 the circulation response in the SST+SIC perturbation runs (contour in Fig. 9e,f). Neither SST  
420 perturbation nor SIC perturbation can reproduce the dipole-like pressure response over the  
421 North Atlantic and the pressure response over the high-latitude Eurasia (Fig. 9a–d). The non-  
422 linear effect of the pressure responses to the SST and SIC perturbations is also strong in the  
423 high-latitude Eurasia, East Asia and the Arctic upper troposphere. The above results suggest  
424 that the pressure response in the SST+SIC perturbation runs of IFS is due to the non-linear  
425 effect of the SST and SIC perturbations.

426 The SLP responses of CAM4 and IFS in the SST perturbation runs are consistent in the  
427 North Pacific (Fig. 8a and Fig. 9a), and match the sign of the inter-model regression pattern  
428 from the ten CMIP5 models albeit with a westward shift (Fig. 4a). The SST perturbation causes  
429 substantial weakening in the Hadley cell and a stronger ITCZ in the northern tropics (Fig. 10).  
430 Regionally, the rainfall is enhanced in the northern tropical Pacific (Fig. 11a,b). This  
431 accompanies stronger divergence over the tropics and stronger convergence over the  
432 midlatitudes at the 250 hPa, representing stronger tropical–midlatitude interaction over the  
433 North Pacific (Fig. 11c,d). The anticyclonic Rossby wave source is enhanced at the region with  
434 a larger gradient in the velocity potential at 15°N (Fig. 11c,d), which is associated with  
435 emanation of the wave activity fluxes from the Pacific to North America (Fig. 11e,f).

436 Indeed, the wave activity fluxes are also emanated from the mid-latitude region with  
437 positive eddy height response (Fig. 11e,f). The increase in the eddy height is partly related to  
438 the tropical midlatitude interactions near the central North Pacific, where stronger convergent  
439 wind corresponds to a cyclonic Rossby wave source (Fig. 11c,d). In CAM4, part of the increase  
440 in the eddy height is related the low-frequency transient eddy forcing, where the convergence  
441 of  $\mathbf{E}$  vector near 30°N,180° corresponds to an easterly wind anomaly associated with the  
442 positive height anomaly (Fig. S6c). In IFS, the Rossby wavetrain propagates equatorward from

443 the northwestern Pacific (Fig. 11f), which is different from the results in its SST+SIC  
444 perturbation runs (Fig. 7f) and the CAM4 runs (Fig. 11e). This again suggests that the dynamics  
445 for the responses of CAM4 and IFS are different. Despite that, the above results suggest that  
446 the SST perturbation from the North Pacific contributes to the high-pressure response over the  
447 North Pacific and the response of Rossby wave propagation from the North Pacific to North  
448 America.

449 In addition to the positive SLP response over the North Pacific, the two AGCMs simulate  
450 consistently a negative SLP response over the mid-latitude North Atlantic in the SST  
451 perturbation runs (Fig. 8a and Fig. 9a). However, their responses in the SST perturbation runs  
452 are different over the continents and the Arctic. On one hand, IFS has a stronger response of  
453 the zonal-mean mass streamfunction to the SST perturbation than CAM4, where the Ferrel and  
454 polar cells weaken and shift northward albeit not statistically significant (Fig. 10b). The  
455 associated weakening of the rising motion in the subpolar latitudes around 70°N is accompanied  
456 by an increase in pressure over the subpolar region across the Canadian Archipelago and the  
457 North Atlantic (Fig. 9a,b). On the other hand, CAM4 does not have responses in the Ferrel and  
458 polar cells to the SST perturbation (Fig. 10a); its midlatitude circulation response is mainly  
459 explained by the wavetrain response (Fig. 11e).

460 In response to the SIC perturbation, the two AGCMs simulate consistently a negative SLP  
461 response over the Arctic (Fig. 8e and Fig. 9e). However, their response outside the Arctic  
462 diverges, including over the North Pacific, Scandinavia and the Mediterranean. That is, the  
463 difference in these SLP responses between the two AGCMs is statistically significant. There is  
464 no consistent response in the meridional circulations (figures not shown). Because SIC does not  
465 robustly influence the midlatitude circulation, we do not analyze in-depth the regional  
466 circulation features over the mid-latitudes and the associated dynamics.

## 467 **5. Summary and conclusions**

### 468 **5.1 Summary**

469 We have identified a pattern that characterizes the uncertainty in the forced SLP response  
470 of ten CMIP5 models ( $PA_{\Delta SLP}$ ). The centers of action of the SLP uncertainty are located at the  
471 northeastern Pacific and the northeastern Atlantic. The positive sign of  $PA_{\Delta SLP}$  is associated  
472 with (i) increasing SLP over the northeastern Pacific and decreasing SLP over the North  
473 American continent, (ii) increasing SLP over the northeastern Atlantic and Scandinavia and  
474 decreasing SLP near the Mediterranean, (iii) decreasing SLP over the Arctic. This pattern also  
475 covaries with uncertainty in forced response of the inter-hemispheric SST gradient, the zonal  
476 SST gradient over the equatorial Pacific and the total Arctic sea ice extent. We have analyzed  
477 the dynamics underlying  $PA_{\Delta SLP}$  and performed sensitivity experiments with two AGCMs to  
478 identify forcing from corresponding global SST and Arctic SIC patterns. The main results are  
479 summarized as follows:

#### 480 5.1.1 Ocean–atmosphere interaction associated with the North Pacific SLP response

481 In the ten CMIP5 models the North Pacific SLP response is associated with the tropical–  
482 midlatitude interactions. Such a SLP response can be better explained by the SST perturbation,  
483 except that the response in two AGCMs is shifted westward. In these AGCM simulations and  
484 the ten CMIP5 models, the SLP response is associated with weakening in the Hadley cell and  
485 the northward shift of ITCZ, where rainfall is enhanced over the tropical northeastern Pacific  
486 with anomalous SST warming. The rainfall response accompanies stronger divergent flow in  
487 the tropical northeastern Pacific and stronger convergent flow in the midlatitude North Pacific.  
488 The stronger convergent flow is partly related to the positive SLP response over the North  
489 Pacific. The anticyclonic Rossby wave source is enhanced in the region with a stronger gradient  
490 in velocity potential. This is associated with a Rossby wavetrain propagating eastward towards

491 North America. The westward shift of the SLP response in CAM4 relative to the CMIP5 forced  
492 response is found to be related to the low-frequency transient eddy forcing.

493 The total SLP response of IFS in the SST+SIC perturbation runs is not the linear sum of the  
494 pressure responses in the SST perturbation runs and the SIC perturbation runs. In contrast, in  
495 CAM4 both the SST and SIC perturbation causes positive SLP responses over the midlatitude  
496 North Pacific, which is stronger in the SST perturbation runs. Therefore, the North Pacific SLP  
497 responses of the two AGCMs in the SST+SIC perturbation runs have different dynamic  
498 mechanisms. Whereas the responses of CAM4 are related to the tropical–midlatitude  
499 interactions and the low-frequency transient eddy forcing driven by the SST perturbation, the  
500 responses of IFS are affected by non-linear dynamics in response to the SST and SIC  
501 perturbations. The CAM4 response and its associated dynamics are closer to the CMIP5 inter-  
502 model regression, suggesting that the forced SLP uncertainty over the northeastern Pacific from  
503 the ten CMIP5 models is associated with the tropical–midlatitude interaction related to the SST  
504 uncertainty over the Pacific.

#### 505 5.1.2 Dipole-like pressure response over the Euro-Atlantic region

506 In the ten CMIP5 models the dipole-like SLP response in the North Atlantic appears to result  
507 from both local response to SST and remote influences from the Pacific. In CAM4, the SLP  
508 responses in the SST perturbation runs and the SST+SIC perturbation runs are similar and again  
509 show some correspondence to the ten CMIP5 SLP uncertainty pattern. In these CAM4  
510 simulations, the Rossby wavetrain simulated in the SST perturbation runs is triggered by SST  
511 over the Pacific. This is consistent with the results of Delcambre et al. (2013), Ciasto et al.  
512 (2016) and Gan et al. (2017). The Atlantic response of CAM4 shifts westward relative to the  
513 CMIP5 inter-model difference, which is probably related to the westward shift in its Pacific  
514 response. On the other hand, IFS also simulates a dipole-like SLP response in the SST+SIC

515 perturbation runs, but such a response is not associated with the Rossby wavetrain propagating  
516 from the North Pacific. Rather, the response is associated with local air-sea interactions over  
517 the midlatitude North Atlantic. The North Atlantic SLP response of IFS in the SST+SIC  
518 perturbation runs is not a linear sum of the responses in the SST perturbation runs and the SIC  
519 perturbation runs. The non-linear dynamics are crucial in the IFS responses.

520 Although the dynamics of the North Atlantic SLP response in the two AGCMs are different,  
521 both AGCMs simulate the positive SLP response near Greenland and the entire dipole-like  
522 response in the SST+SIC perturbation runs only. The forced SLP uncertainty over the  
523 northeastern Atlantic from the ten CMIP5 models appears to be affected by the combined  
524 influence of the uncertainty in SST and SIC.

### 525 5.1.3 Diverging midlatitude response to Arctic sea ice

526 The SLP responses of the two AGCMs to the SIC perturbation are consistent in the Arctic  
527 and show lower SLP associated with less sea ice, as in the ten CMIP5 models. However, the  
528 midlatitude SLP response of the two AGCMs diverges. Because the difference in the  
529 midlatitude SLP response between the two AGCMs is statistically significant (Fig. S8), we do  
530 not expect their midlatitude response to SIC would become consistent even if the simulation is  
531 extended to 100 years or longer. The above results in turn suggest a limited direct impact of  
532 SIC on the midlatitudes, consistent with Ogawa et al. (2018). Indeed, the midlatitude circulation  
533 could affect the SIC. For example, an extra-tropical anticyclone (e.g., blocking) could enhance  
534 the advection of warm air towards the polar region and reduces the SIC (Gong and Luo 2017;  
535 Svendsen et al. 2018). This linkage could explain the relation in the ten CMIP5 models, but this  
536 cannot be verified in the AGCM experiments and this is beyond the scope of this study.

537 Previous studies have shown that the midlatitude circulation response to SIC could be  
538 amplified by the stratosphere (Zhang et al. 2018; De and Wu 2019). However, the regression

539 of  $PA_{\Delta SLP}$  against the forced response in the DJF 10-hPa height is not statistically significant  
540 (Fig. 12a). That means the uncertainty in the forced response of the stratospheric polar vortex  
541 is not considerably correlated to  $PA_{\Delta SLP}$ . Consistently, the stratospheric response to the SIC  
542 perturbation in the two AGCMs has small signal-to-noise ratios (Fig. 12f,g). Compared to  
543 CAM4, IFS has a much higher model top and its stratospheric dynamics might be better  
544 resolved, but the stratospheric responses of IFS to the SST perturbation and the SST+SIC  
545 perturbation are weaker than CAM4 (Fig. 12b–e). Therefore, the impact of stratosphere on the  
546 tropospheric circulation is not apparent in this study. Note that the results in this study are  
547 related to the uncertainty in the forced SLP responses over the northeastern Pacific and the  
548 northeastern Atlantic (i.e.,  $PA_{\Delta SLP}$ ). The weak linkage between  $PA_{\Delta SLP}$  and the stratospheric  
549 circulation does not imply the uncertainty in the forced response of the tropospheric circulation  
550 being unrelated to the stratospheric circulation in other models. Our results could also be  
551 affected by the small number of high-top models (three out of ten models) (Charlton-Perez et  
552 al. 2013) and the perturbation pattern of the Arctic SIC in this study.

## 553 **5.2 Conclusions**

554 The future projection of the winter SLP in the northeastern Pacific and the northeastern  
555 Atlantic has a large inter-model spread, which covaries with the large-scale SST gradients and  
556 the total Arctic sea ice extent. In this study, the sensitivity experiments of CAM4 and IFS  
557 revealed that atmospheric responses to the same SST and SIC boundary conditions are generally  
558 large, with more coherent responses over the oceans (in terms of the sign of response) and less  
559 coherent remote responses to these boundary conditions. Specifically, we have learnt the  
560 following points:

- 561 • The uncertainty in the forced SLP response over the northeastern Pacific is about twice as  
562 large as the uncertainty related to internal climate variability. This uncertainty is better  
563 explained by the SST perturbation, and it is associated with tropical-midlatitude  
564 interactions and the propagation of a Rossby wavetrain towards North America. The  
565 relative contribution from the tropical and extratropical Pacific should be investigated in  
566 future;
- 567 • The uncertainty in the forced SLP response over the northeastern Atlantic is of similar  
568 strength as internal climate variability and is even weaker than it at high latitudes. This  
569 uncertainty is better explained by the joint effect of SST and SIC perturbations. It appears  
570 to be related to a Rossby wavetrain from the North Pacific and with local air-sea  
571 interactions, with the first more important in CAM4 and the second more important in IFS;
- 572 • The uncertainties over the northern hemisphere continents and at high latitudes appear to  
573 depend sensitively on the atmospheric model. Furthermore, the response to SST and SIC  
574 perturbations can be non-linear in some models (e.g., IFS), while quite linear in others (e.g.,  
575 CAM4). Thus, we should be cautious when using single climate model to understand the  
576 physical mechanism responsible for the uncertainty in future climate projections from  
577 multiple models;
- 578 • Future projections of the winter SLP might not be improved by constraining only the SST  
579 and SIC projections. We should investigate other factors contributing to the inter-model  
580 spread in the winter SLP (e.g., the atmosphere–SST–SIC coupled dynamics) in order to  
581 provide more accurate climate projections.

582 One limitation of our study is that the uncertainty in future climate projections is computed  
583 from only ten CMIP5 models with only three ensemble members, where these models have  
584 more substantial weakening in the Icelandic low than the whole CMIP5 models. The SLP

585 pattern from the inter-model EOF analysis, as well as the corresponding SST and SIC patterns,  
586 might also be sensitive to the number of models. To reduce uncertainties related to internal  
587 variability and to make the analysis more representative, more models with more ensemble  
588 members are required to separate the forced response from the internal climate variability,  
589 especially for the northeastern Atlantic and the Arctic. Nevertheless, we believe the results here  
590 should motivate further studies to understand the inter-model spread of the future climate  
591 projections. Our results suggest it is important to better assess the relative contribution of  
592 tropical and extratropical SST to the spread in future climate projections, as well as the role of  
593 the eddy forcing. It is also important to study the role of ocean dynamics (Woollings et al. 2012;  
594 Omrani et al. 2016), the troposphere–stratosphere interaction (Manzini et al. 2014; Omrani et  
595 al. 2014; De and Wu 2019), internal climate variability (Deser et al. 2012, 2020) and forced  
596 variability to the future climate projections, especially over the North Atlantic and high latitudes.

597 **Acknowledgments:** This work began when HNC was a postdoctoral fellow at the  
598 University of Bergen. This study was supported by the NordForsk ARCPATH and TRACE  
599 projects (#76654; #90077). HNC was supported by Guangdong Province Key Laboratory for  
600 Climate Change and Natural Disaster Studies (Grant No. 2020B1212060025), the National Key  
601 Research and Development Program of China (Grant No. 2016YFA0600704), and the National  
602 Natural Science Foundation of China (Grant No. 42088101, 41905050); NK was supported by  
603 the EU H2020 ERC programme under the STERCP (Grant No. 648982) project; SQ was  
604 supported by the National Natural Science Foundation of China (Grant No. 41905057); ZW  
605 was supported by the Center for Ocean Research in Hong Kong and Macau (CORE).  
606 Computing resources were provided by UNITETT Sigma AS (NN2343K, NN9390K,  
607 NS9015K, NS9064K). The computations with IFS were performed on resources provided by

608 the Swedish National Infrastructure for Computing (SNIC) at the National Supercomputing  
609 Centre at Linköping University (NSC).

610 **Data availability statement:** The CAM4 and IFS data will be available upon request and  
611 will be located on the National Infrastructure for Research Data (NIRD) in Norway.

## 612 **References**

- 613 Andrew T, Gregory J, Webb M, Taylor K (2012) Forcing, feedbacks and climate sensitivity in  
614 CMIP5 coupled atmosphere-ocean climate models. *Geophys Res Lett* 39:L09712.  
615 <https://doi.org/10.1029/2012GL051607>
- 616 Bader J, Mesquita MDS, Hodges KI, Keenlyside N, Østerhus S, Miles M (2011) A review on  
617 Northern Hemisphere sea-ice, storminess and the North Atlantic Oscillation: Observations  
618 and projected changes. *Atmos Res* 101:809–834
- 619 Balsamo GP, Beljaars A, Scipal K, Viterbo P, Hurk B, Hirschi M, Betts AK (2009) A revised  
620 hydrology for the ECMWF model: Verification from field site to terrestrial water storage  
621 and impact in the integrated forecast system. *J Hydrometeorology* 10:623–643.  
622 <https://doi.org/10.1175/2008JHM1068.1>
- 623 Barnes EA, Polvani L (2013) Response of the midlatitude jets, and of their variability, to  
624 increased greenhouse gases in the CMIP5 models. *J Climate* 26:7117–7135.  
625 <https://doi.org/10.1175/JCLI-D-12-00536.1>
- 626 Barnes EA, Screen J (2015) The impact of Arctic warming on the midlatitude jet-stream: Can  
627 it? Has it? Will it? *Wiley Interdiscip Rev: Climate Change* 6:277–286.  
628 <https://doi.org/10.1002/wcc.337>
- 629 Blackport R, Kushner PJ (2017) Isolating the atmospheric circulation response to Arctic sea ice  
630 loss in the coupled climate system. *J Climate* 30:2163–2185. [https://doi.org/10.1175/JCLI-](https://doi.org/10.1175/JCLI-D-16-0257.1)  
631 [D-16-0257.1](https://doi.org/10.1175/JCLI-D-16-0257.1)
- 632 Cattiaux J, Cassou C (2013) Opposite CMIP3/CMIP5 trends in the wintertime Northern  
633 Annular Mode explained by combined local sea ice and remote tropical influences. *Geophys*  
634 *Res Lett* 40:3682–3687. <https://doi.org/10.1002/grl.50643>
- 635 Chang EKM., Guo Y, Xia X (2012) CMIP5 multimodel ensemble projection of storm track  
636 change under global warming. *J Geophys Res* 117:D23118.  
637 <https://doi.org/10.1029/2012JD018578>
- 638 Charlton-Perez A, Baldwin MP, Birner T et al (2013) On the lack of stratospheric dynamical  
639 variability in low-top versions of the CMIP5 models. *J Geophys Res* 118:2494–2505.  
640 <https://doi.org/10.1002/jgrd.50125>
- 641 Cheung HHN, Keenlyside NS, Omrani NE, Zhou W (2018) Remarkable link between projected  
642 uncertainties of Arctic sea ice decline and winter Eurasian climate. *Adv Atmos Sci* 35:38–  
643 51. <https://doi.org/10.1007/s00376-017-7156-5>
- 644 Choi J, Lu J, Son SW, Frierson DM, Yoon JH (2016) Uncertainty in future projections of the  
645 North Pacific subtropical high and its implication for California winter precipitation  
646 change. *J Geophys Res Atmos* 121:795–806. <https://doi.org/10.1002/2015JD023858>

- 647 Ciasto LM, Li C, Wettstein JJ, Kvamstø NG (2016) North Atlantic storm-track sensitivity to  
648 projected sea surface temperature: Local versus remote influences. *J Climate* 29:6973–  
649 6991. <https://doi.org/10.1175/JCLI-D-15-0860.1>
- 650 Collins M, Knutti R, Arblaster J, Dufresne J-L, Fichefet T, Friedlingstein P, Gao X, Gutowski  
651 WJ, Johns T, Krinner G, Shongwe M, Tebaldi C, Weaver AJ, Wehner M (2013) Long-  
652 term climate change: projections, commitments and irreversibility. In: Stocker TF, Qin D,  
653 Plattner G-K, Tignor M, Allen SK, Boschung J, Nauels A, Xia Y, Bex V, Midgley PM  
654 (eds) *Climate change 2013: the physical science basis. Contribution of Working Group I  
655 to the Fifth Assessment Report of the Intergovernmental Panel on Climate Change.*  
656 Cambridge University Press, Cambridge
- 657 De B., Wu Y (2019) Robustness of the stratospheric pathway in linking the Barents-Kara sea  
658 variability to the mid-latitude circulation in CMIP5 models. *Climate Dyn* 53:193–207.  
659 <https://doi.org/10.1007/s00382-018-4576-6>
- 660 Delcambre SC, Lorenz DJ, Vimont DJ, Martin JE (2013) Diagnosing Northern Hemisphere jet  
661 portrayal in 17 CMIP3 global climate models: Twenty-first-century projections. *J Climate*  
662 26:4930–4946. <https://doi.org/10.1175/JCLI-D-12-00359.1>
- 663 Deser C, Phillips A, Bourdette V, Teng H (2012) Uncertainty in climate change projections:  
664 The role of internal variability. *Climate Dyn* 38:527–546. [https://doi.org/10.1007/s00382-  
665 010-0977-x](https://doi.org/10.1007/s00382-010-0977-x)
- 666 Deser C, Tomas RA, Sun L (2015) The role of ocean–atmosphere coupling in the zonal-mean  
667 atmospheric response to Arctic sea ice loss. *J Climate* 28:2168–2186.  
668 <https://doi.org/10.1175/JCLI-D-14-00325.1>
- 669 Deser C, Sun L, Tomas RA, Screen J (2016) Does ocean coupling matter for the northern  
670 extratropical response to projected Arctic sea ice loss? *Geophys Res Lett* 43:2149–2157.  
671 <https://doi.org/10.1002/2016GL067792>
- 672 Deser C, Lehner F, Rodgers KB et al (2020) Insights from Earth system model initial-condition  
673 large ensembles and future prospects. *Nat Climate Change* 10:277–286.  
674 <https://doi.org/10.1038/s41558-020-0731-2>
- 675 Ding Q, Wallace JM, Battisti DS, Steig EJ, Gallant AJE, Kim HJ, Geng L (2014) Tropical  
676 forcing of the recent rapid Arctic warming in northeastern Canada and Greenland. *Nature*  
677 509:209–223. <https://doi.org/10.1038/nature13260>
- 678 Gan B, Wu L, Jia F, Li S, Cai W, Nakamura H, Alexander MA, Miller AJ (2017) On the  
679 response of the Aleutian low to greenhouse warming. *J Climate* 30:3907–3925.  
680 <https://doi.org/10.1175/JCLI-D-15-0789.1>
- 681 Gervais M, Shaman J, Kushnir Y (2019) Impacts of the North Atlantic warming hole in future  
682 climate projections: Mean atmospheric circulation and the North Atlantic jet. *J Climate*  
683 32:2673–2689. <https://doi.org/10.1175/JCLI-D-18-0647.1>
- 684 Gong T, Luo D (2017) Ural blocking as an amplifier of the Arctic sea ice decline in winter. *J*  
685 *Climate* 30:2639–2654. <https://doi.org/10.1175/JCLI-D-16-0548.1>
- 686 Hand R, Keenlyside NS, Omrani NE, Bader J, Greatbatch RJ (2019) The role of local sea  
687 surface temperature pattern changes in shaping climate change in the North Atlantic sector.  
688 *Clim Dyn* 52:417–438. <https://doi.org/10.1007/s00382-018-4151-1>
- 689 Harvey BJ, Shaffrey LC, Woollings TJ (2015) Deconstructing the climate change response of  
690 the Northern Hemisphere wintertime storm tracks. *Clim Dyn* 45: 2847–2860.  
691 <https://doi.org/10.1007/s00382-015-2510-8>

692 Hazeleger W, Severijns C, Semmler T (2010) EC-Earth: a seamless earth system prediction  
693 approach in action. *Bull Amer Meteor Soc* 91:1357–1363.  
694 <https://doi.org/10.1175/2010BAMS2877.1>

695 Horel JD, Wallace JM (1981) Planetary-scale atmospheric phenomena associated with the  
696 Southern Oscillation. *Mon Wea Rev* 109:813–829

697 Hoskins BJ, Valdes PJ (1990) On the existence of storm-tracks. *J Atmos Sci* 47:1854–1864

698 Hu X, Taylor PC, Cai M, Yang S, Deng Y, Sejas S (2017) Inter-model warming projection  
699 spread: Inherited traits from control climate diversity. *Sci Rep* 7:4300.  
700 <https://doi.org/10.1038/s41598-017-04623-7>

701 Hu X, Fan H, Cai M, Sejas SA, Taylor P, Yang S (2020) A less cloudy picture of the inter-  
702 model spread in future global warming projections. *Nat Comm* 11:4472,  
703 <https://doi.org/10.1038/s41467-020-18227-9>

704 Kang SM, Frierson DMW, Held IM (2009) The tropical response to extratropical thermal  
705 forcing in an idealized GCM: The importance of radiative feedbacks and convective  
706 parameterization. *J Atmos Sci* 66:2812–2827

707 Lau NC (1988) Variability of the observed midlatitude storm tracks in relation to low-frequency  
708 changes in the circulation pattern. *J Atmos Sci* 45:2718–2743

709 Lau NC, Ploshay JJ (2013) Model projections of the changes in atmospheric circulation and  
710 surface climate over North America, the North Atlantic, and Europe in the twenty-first  
711 century. *J Climate* 26:9603–9620. <https://doi.org/10.1175/JCLI-D-13-00151.1>

712 Manzini E, Yu. Karpechko A, Anstey J et al (2014) Northern winter climate change:  
713 Assessment of uncertainty in CMIP5 projections related to stratosphere-troposphere  
714 coupling. *J. Geophys. Res.*, 119, 7979–7998. <https://doi.org/10.1002/2013JD021403>

715 Neale RB, Richter J, Park S, Lauritzen PH, Vavrus SJ, Rasch PJ, Zhang M (2013) The mean  
716 climate of the Community Atmosphere Model (CAM4) in forced SST and fully coupled  
717 experiments. *J Climate* 26:5150–5168. <https://doi.org/10.1175/JCLI-D-12-00236.1>

718 Ogawa F, Keenlyside N, Gao Y et al (2018) Evaluating impacts of recent Arctic sea-ice loss on  
719 the northern hemisphere winter climate change. *Geophys Res Lett* 45:3255–3263.  
720 <https://doi.org/10.1002/2017GL076502>

721 Omrani NE, Keenlyside NS, Bader J, Manzini E (2014) Stratospheric key for wintertime  
722 atmospheric response to warm Atlantic decadal conditions. *Climate Dyn* 42:649–663

723 Omrani NE, Bader J, Keenlyside NS, Manzini E (2016) Troposphere-stratosphere response to  
724 large-scale North Atlantic ocean variability in an atmosphere/ocean coupled model.  
725 *Climate Dyn* 46:1397–1415. <https://doi.org/10.1007/s00382-015-2654-6>

726 Oudar T, Cattiaux J, Douville H (2020) Drivers of the Northern extratropical eddy-driven jet  
727 change in CMIP5 and CMIP6 models. *Geophys Res Lett* 47: e2019GL086695.  
728 <https://doi.org/10.1029/2019GL086695>

729 Peings Y, Magnusdottir G (2014) Response of the wintertime Northern Hemisphere  
730 atmospheric circulation to current and projected Arctic sea ice decline: A numerical study  
731 with CAM5. *J Climate* 27:244–264. <https://doi.org/10.1175/JCLI-D-13-00272.1>

732 Sardeshmukh PD, Hoskins BJ (1988) The generation of global rotational flow by steady  
733 idealized tropical divergence. *J Atmos Sci* 45:1228–1251

734 Schneider T, Bischoff T, Haug GH (2014) Migrations and dynamics of the intertropical  
735 convergence zone. *Nature* 513:45–53

- 736 Screen J A, Simmonds I, Deser C, Tomas R (2013) The atmospheric response to three decades  
737 of observed Arctic sea ice loss. *J Climate* 26:1230–1248. [https://doi.org/10.1175/JCLI-D-](https://doi.org/10.1175/JCLI-D-12-00063.1)  
738 12-00063.1
- 739 Shaw TA, Baldwin M, Barnes EA et al (2016) Storm track processes and the opposing influence  
740 of climate change. *Nat Geoscience* 9:656–664. <https://doi.org/10.1038/ngeo2783>
- 741 Shepherd TG (2014) Atmospheric circulation as a source of uncertainty in climate change  
742 projections. *Nat Geoscience* 7:703–708. <https://doi.org/10.1038/NGEO2253>
- 743 Svendsen L, Keenlyside N, Bethke I, Gao Y, Omrani NE (2018) Pacific contribution to the  
744 early twentieth century warming in the Arctic. *Nat Clim Change* 8:793–797.  
745 <https://doi.org/10.1038/s41558-018-0247-1>
- 746 Takaya K, Nakamura H (2001) A formulation of a phase-independent wave-activity flux for  
747 stationary and migratory quasi-geostrophic eddies on a zonally-varying basic flow. *J*  
748 *Atmos Sci* 58:608–627
- 749 Taylor PC, Cai M, Hu A, Meehl J, Washington W, Zhang GJ (2013) A decomposition of  
750 feedback contribution to polar warming amplification. *J Climate* 26:7023–7043.  
751 <https://doi.org/10.1175/JCLI-D-12-00696.1>
- 752 Vial J, Dufresne JL, Bony S (2013) On the interpretation of inter-model spread in CMIP5  
753 climate sensitivity estimates. *Clim Dyn* 41:3339–3362. [https://doi.org/10.1007/s00382-](https://doi.org/10.1007/s00382-013-1725-9)  
754 013-1725-9
- 755 Woollings T, Gregory JM, Pinto JG, Reyers M, Brayshaw DJ (2012) Response of the North  
756 Atlantic storm track to climate change shaped by ocean-atmosphere coupling. *Nat*  
757 *Geoscience* 5:313–317. <https://doi.org/10.1038/NGEO1438>
- 758 Yim BY, Min HS, Kug JS (2016) Inter-model diversity in jet stream changes in relation to  
759 Arctic climate in CMIP5. *Clim Dyn* 47:235–248. [https://doi.org/10.1007/s00382-015-](https://doi.org/10.1007/s00382-015-2833-5)  
760 2833-5
- 761 Yin JH (2005) A consistent poleward shift of the storm tracks in simulations of 21st century  
762 climate. *Geophys Res Lett* 32:L1870. <https://doi.org/10.1029/2005GL023684>.
- 763 Zappa G, Shepherd TG (2017) Storylines of atmospheric circulation change for European  
764 climate impact assessment. *J Climate* 30:6561–6577. [https://doi.org/10.1175/JCLI-D-16-](https://doi.org/10.1175/JCLI-D-16-0807)  
765 0807
- 766 Zappa G, Pithan F, Shepherd TG (2018) Multimodel evidence for an atmospheric circulation  
767 response to Arctic sea ice loss in the CMIP5 future projections. *Geophys Res Lett* 45:1011–  
768 1019. <https://doi.org/10.1002/2017GL076096>
- 769 Zhang P, Wu Y, Simpson IR, Smith KL, Zhang X, De B, Callaghan P (2018) A stratospheric  
770 pathway linking a colder Siberia to Barents-Kara sea ice loss. *Sci Advances* 4:eaat6025.  
771 <https://doi.org/10.1126/sciadv.aat6025>

772

## List of Tables

773 Table 1. List of CMIP5 coupled models.

774 Table 2. List of AGCM sensitivity experiments. \*For grids in the Northern Hemisphere with  
775  $|\text{SIC}_{\Delta\text{SLP}}| \geq 0.1$  (fraction),  $\text{SST}_{\Delta\text{SLP}}$  changes consistently with SIC (see text for details).

777 Fig. 1. Multi-model mean (MME) of the DJF sea level pressure (SLP) in 1971/72–2000/01 of  
 778 the historical run (contour), and the forced response (shading) based on ten CMIP5 models  
 779 listed in Table 1: (a) the MME forced response, where gray dots and black dots indicate  
 780 the regions that at least seven and nine out of ten models agree on the sign of MME change,  
 781 (b) the uncertainty in the forced response (inter-model standard deviation of the projection),  
 782 where dots indicate the regions that the uncertainty is significantly larger than the internal  
 783 climate variability at the 90% confidence level of  $F$ -test, (c) the internal climate variability  
 784 (intra-model standard deviation of the projection), where dots indicate the regions where  
 785 the internal climate variability is significantly larger than the uncertainty at the 90%  
 786 confidence level of  $F$ -test. Unit: hPa.

787 Fig. 2. (a)–(b) First two eigenvectors (EOF1 and EOF2; shading) and the uncertainty (inter-  
 788 model standard deviation; contour) in the forced DJF SLP response of the ten CMIP5  
 789 models, (c) As in (a)–(b), but for the sum of EOF1 and EOF2, which is called the Pacific–  
 790 Atlantic SLP uncertainty pattern ( $PA_{\Delta SLP}$ ), (d) the inter-model relationship between the  
 791 forced SLP response over the northeastern Atlantic ( $60^{\circ}$ – $85^{\circ}$ N and  $20^{\circ}$ W– $10^{\circ}$ E) and over  
 792 the northeastern Pacific ( $40^{\circ}$ – $65^{\circ}$ N and  $160^{\circ}$ – $135^{\circ}$ W), where these regions are represented  
 793 by the black boxes in (a)–(c). Unit: hPa.

794 Fig. 3. (a)–(b) Inter-model regression of the forced response against  $PAI_{\Delta SLP}$  (shading) and the  
 795 uncertainty in the forced response (i.e., inter-model standard deviation; contour) of the ten  
 796 CMIP5 models: (a) SST (contour interval:  $0.4^{\circ}$ C), (b) SIC (contour interval: 0.1 fraction),  
 797 where the outermost circle in the polar stereographic map is  $45^{\circ}$ N. (c)–(e) Scatterplot of  
 798 the inter-model relationship between  $PAI_{\Delta SLP}$  (abscissa) and the future projection  
 799 (ordinate): (c) the equator-to-pole SST gradient, (d) the inter-hemispheric SST gradient, (e)  
 800 the zonal SST gradient between the equatorial western and eastern Pacific ( $^{\circ}$ C), and (f) the  
 801 total Arctic sea ice extent ( $10^6$  km $^2$ ).

802 Fig. 4. Assessing the uncertainty in the DJF forced response of (left) SLP (contour interval: 0.5  
 803 hPa) and (right) 250-hPa geopotential height (contour interval: 10 m) associated with  
 804  $PA_{\Delta SLP}$ . (a)–(b) Inter-model regression of the forced response against  $PAI_{\Delta SLP}$  across the  
 805 ten CMIP5 models. (c)–(f) the AGCM response in the SST+SIC perturbation runs (run1  
 806 minus run2): (c)–(d) CAM4, (e)–(f) IFS. Unit: hPa. Stippling indicates the 90% confidence  
 807 level in the CMIP5 inter-model regression, and the 95% confidence level in AGCM  
 808 experiments based on the two-tailed Student's  $t$ -test.

809 Fig. 5. Assessing the uncertainty in the DJF forced response of the zonal-mean mass  
 810 streamfunction ( $10^9$  kg s $^{-1}$ ) and the zonal-mean precipitation (mm day $^{-1}$ ) associated with  
 811  $PA_{\Delta SLP}$ . (a) Inter-model regression of the forced response against  $PAI_{\Delta SLP}$  across the ten  
 812 CMIP5 models, (b)–(c) the AGCM response in the SST+SIC perturbation runs (run1  
 813 minus run2): (b) CAM4, and (c) IFS. For figures showing the zonal-mean mass  
 814 streamfunction, the contour lines indicate the 2069/70–2098/99 DJF climatology in the  
 815 RCP8.5 scenario, where the thick lines indicate 0, the solid and dashed lines indicate the  
 816 contours  $\pm 5 \times 10^9$  kg s $^{-1}$  and the multiples of  $\pm 25 \times 10^9$  kg s $^{-1}$ . For figures showing the zonal-  
 817 mean precipitation, blue line indicates the CMIP5 inter-model regression or the AGCM  
 818 response, and red line indicates the 2069/70–2098/99 DJF climatology. Stippling and blue  
 819 dots denotes the grid points exceeding the 95% confidence interval of the zonal-mean mass  
 820 streamfunction and the zonal-mean precipitation, respectively.

821 Fig. 6. Inter-model regression of the forced response against  $PAI_{\Delta SLP}$  across the ten CMIP5  
822 models. (a) Precipitation (shading;  $\text{mm day}^{-1}$ ). (b) 250-hPa velocity potential (contour;  $10^5$   
823  $\text{m}^2 \text{s}^{-1}$ ), divergent wind (vector;  $\text{m s}^{-1}$ ), and Rossby wave source (shading;  $10^{-11} \text{s}^{-2}$ ). (c)  
824 250-hPa eddy geopotential height (contour interval: 10 m) and horizontal component of  
825 wave activity fluxes (vector;  $\text{m}^2 \text{s}^{-2}$ ), and Rossby wave source (shading;  $10^{-11} \text{s}^{-2}$ ) Stippling  
826 in (a) indicates the 95% confidence level.

827 Fig. 7. As in Fig. 6, but for the (left) CAM4 and (right) IFS responses in the SST+SIC  
828 perturbation runs.

829 Fig. 8. DJF response of (left) SLP (contour interval: 0.5 hPa) and (right) 250-hPa geopotential  
830 height (contour interval: 10 m) in CAM4. (a)–(b) the SST perturbation runs, and (c)–(d)  
831 the SIC perturbation runs, (e)–(f) the response in the SST+SIC perturbation runs (contour)  
832 and the sum of responses in the SST perturbation runs and the SIC perturbation runs  
833 (shading). In (a)–(d), stippling indicates the 95% confidence level based on the two-tailed  
834 Student's *t*-test.

835 Fig. 9. As in Fig. 8, but for the response in IFS.

836 Fig. 10. As in Fig. 5, but for the response of CAM4 and IFS in the SST perturbation runs.

837 Fig. 11. As in Fig. 6, but for the response in the SST perturbation runs: (left) CAM4 and (right)  
838 IFS.

839 Fig. 12. Assessing the uncertainty in the DJF response of the 10-hPa geopotential height  
840 (contour interval: 30 m) associated with  $PAI_{\Delta SLP}$ . (a) Inter-model regression of the forced  
841 response against  $PAI_{\Delta SLP}$  across the ten CMIP5 models. The response of (middle) CAM4  
842 and (right) IFS in (b)–(c) the SST+SIC perturbation runs (run1 minus run2), (d)–(e) the  
843 SST perturbation runs (run3 minus run4), and (f)–(g) the SIC perturbation runs (run 5  
844 minus run6). Unit: hPa. Shading indicates the 90% confidence level in the CMIP5 inter-  
845 model regression, and the 95% confidence level in AGCM experiments based on the two-  
846 tailed Student's *t*-test.

847 Table 1. List of CMIP5 coupled models.

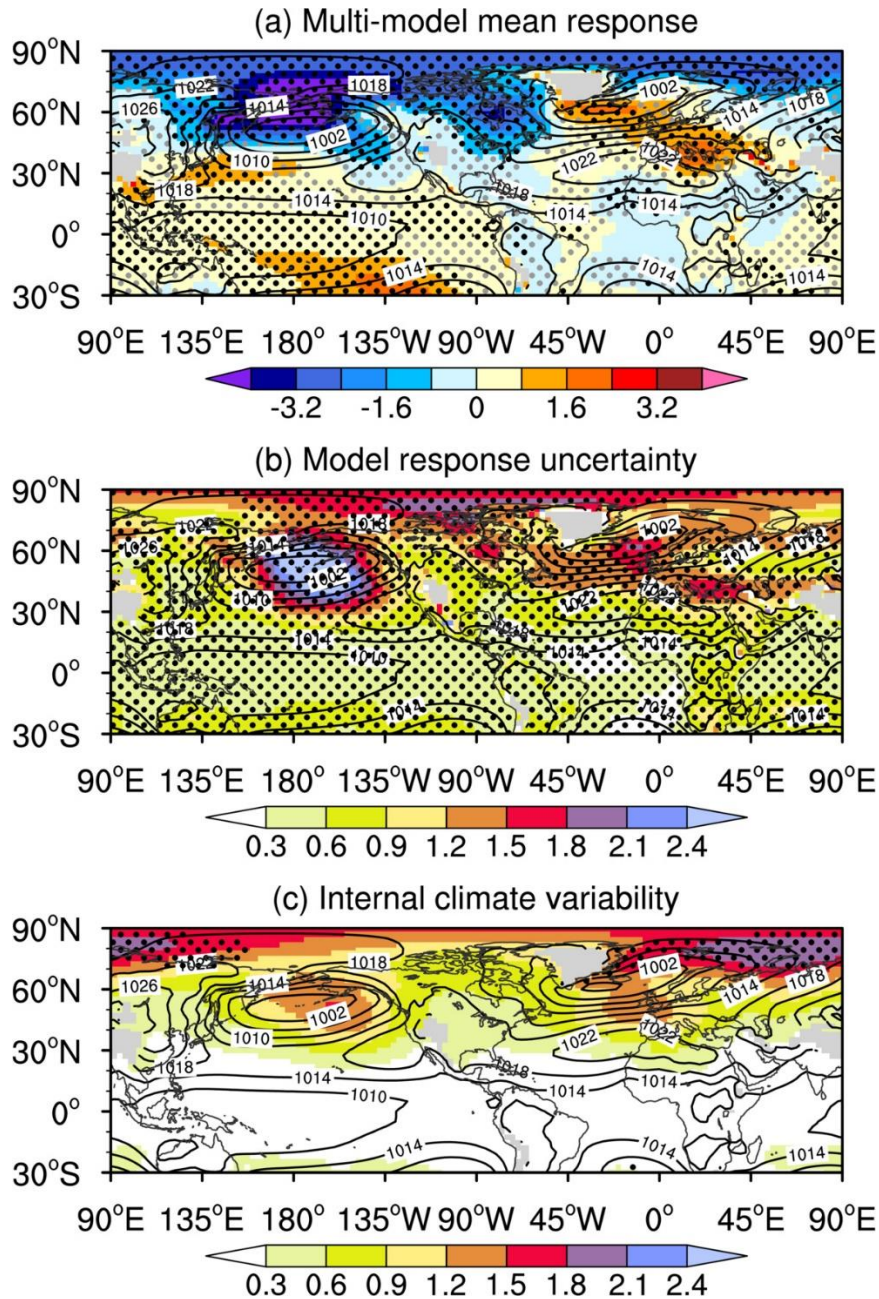
Number	Model	Ensemble members (r{n}i1p1)	Horizontal resolution atmospheric (lat×lon)	of model	Horizontal resolution of ocean model (lat×lon)
1	CanESM2	1–5	2.8°×2.8°		0.9°×1.4°
2	CCSM4	1–6	0.9°×1.3°		0.6°×0.9°
3	CESM1-CAM5	1–3	0.9°×1.3°		0.6°×0.9°
4	CNRM-CM5	1, 2, 4, 6, 10	1.4°×1.4°		0.6°×1.0°
5	FIO-ESM	1–3	2.8°×2.8°		0.5°×1.1°
6	HadGEM2-CC	1–3	1.3°×1.9°		0.8°×1.0°
7	HadGEM2-ES	1–4	1.3°×1.9°		0.8°×1.0°
8	IPSL-CM5A-LR	1–4	1.9°×3.8°		1.2°×2.0°
9	MIROC5	1–3	1.4°×1.4°		0.8°×1.4°
10	MPI-ESM-LR	1–3	1.9°×1.9°		0.8°×1.4°

848

849 Table 2. List of AGCM sensitivity experiments. \*For grids in the Northern Hemisphere with  
 850  $|\text{SIC}_{\Delta\text{SLP}}| \geq 0.1$  (fraction),  $\text{SST}_{\Delta\text{SLP}}$  changes consistently with SIC (see text for details).

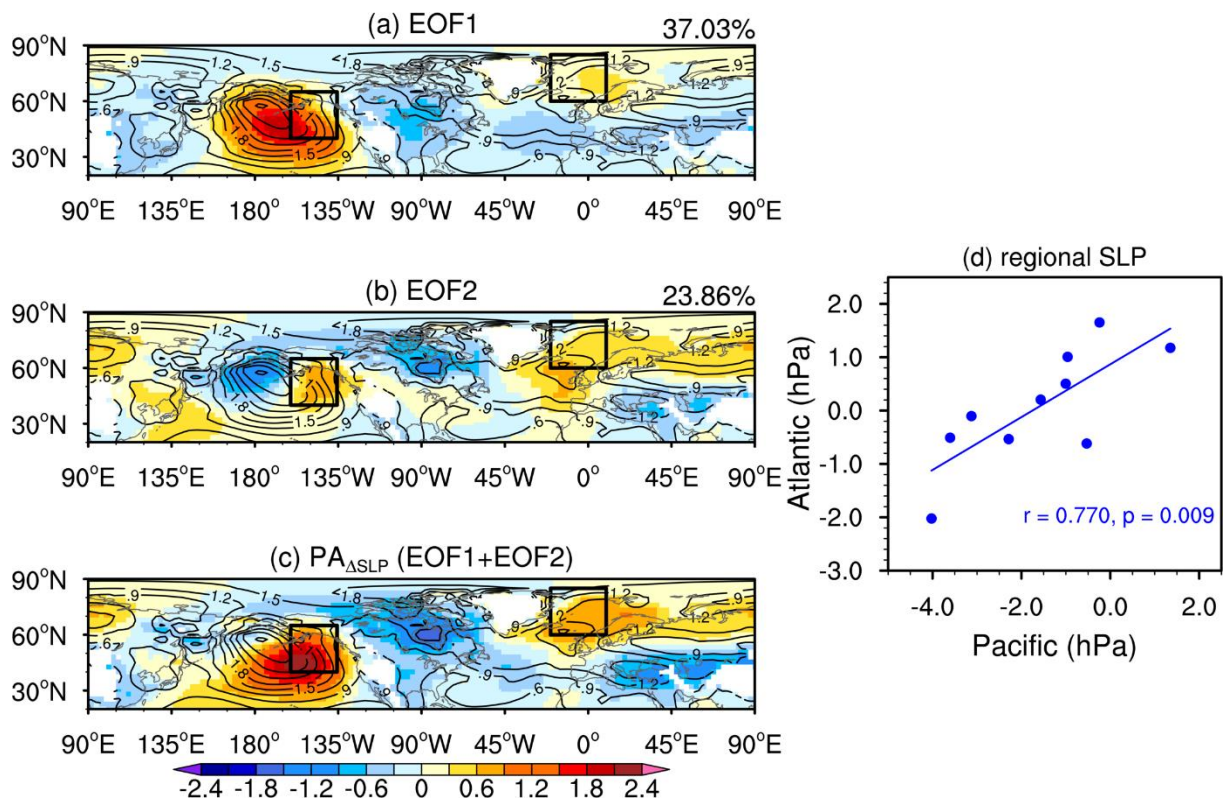
Type	Run	Prescribed monthly-varying SST	Prescribed monthly-varying SIC
SST+SIC perturbation runs	1	2069-2098 MME ( $\text{SST}_{\text{MME}}$ ) + $0.5 \times$ regressed SST pattern ( $\text{SST}_{\Delta\text{SLP}}$ )	2069-2098 MME ( $\text{SIC}_{\text{MME}}$ ) + $0.5 \times$ regressed SIC pattern ( $\text{SIC}_{\Delta\text{SLP}}$ )
	2	$\text{SST}_{\text{MME}} - 0.5 \times \text{SST}_{\Delta\text{SLP}}$	$\text{SIC}_{\text{MME}} - 0.5 \times \text{SIC}_{\Delta\text{SLP}}$
SST perturbation runs	3	$\text{SST}_{\text{MME}} + 0.5 \times \text{SST}_{\Delta\text{SLP}}^*$	$\text{SIC}_{\text{MME}}$
	4	$\text{SST}_{\text{MME}} - 0.5 \times \text{SST}_{\Delta\text{SLP}}^*$	$\text{SIC}_{\text{MME}}$
SIC perturbation runs	5	$\text{SST}_{\text{MME}}^*$	$\text{SIC}_{\text{MME}} + 0.5 \times \text{SIC}_{\Delta\text{SLP}}$
	6	$\text{SST}_{\text{MME}}^*$	$\text{SIC}_{\text{MME}} - 0.5 \times \text{SIC}_{\Delta\text{SLP}}$

851



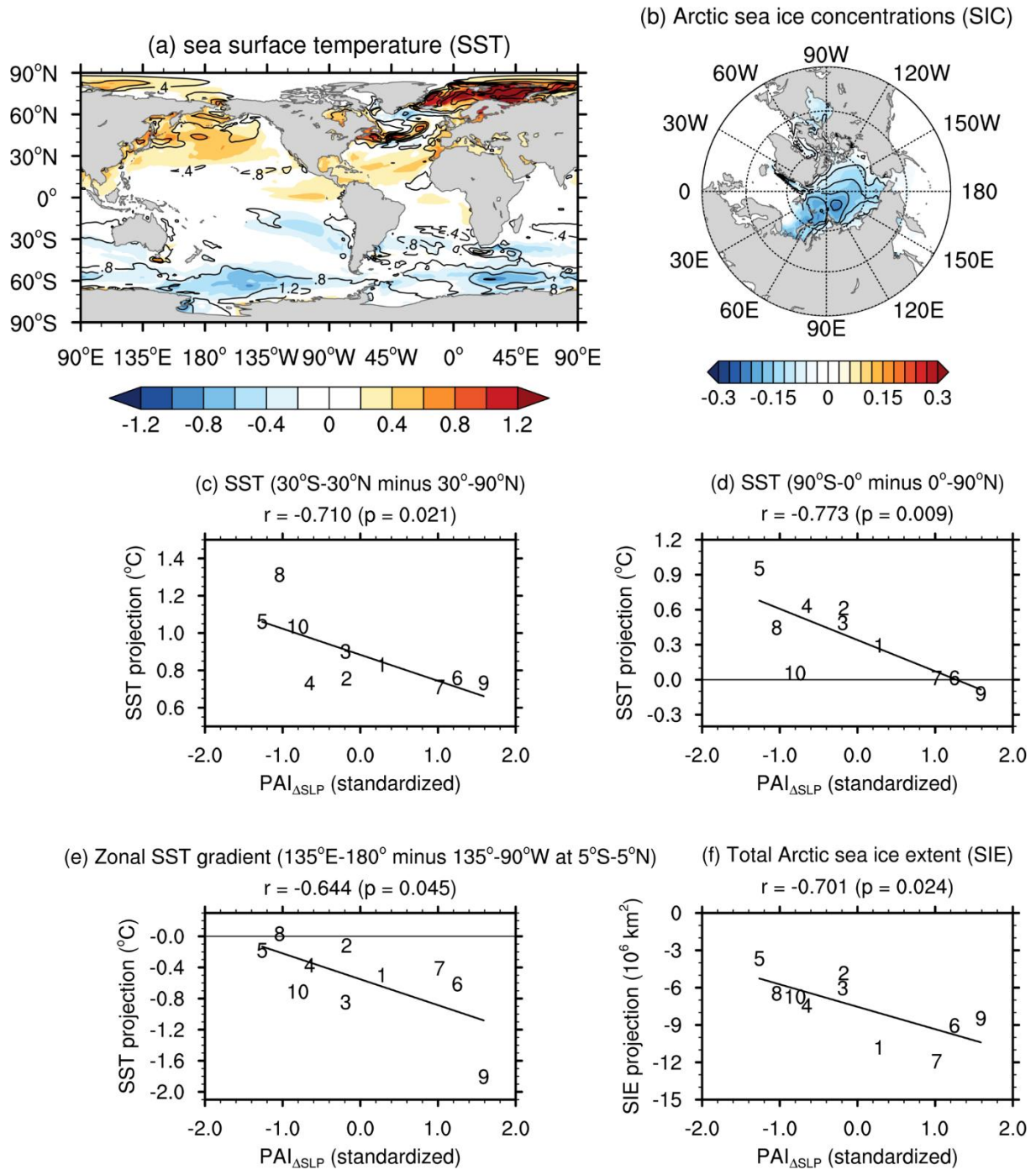
852

853 Fig. 1. Multi-model mean (MME) of the DJF sea level pressure (SLP) in 1971/72–2000/01 of  
 854 the historical run (contour), and the forced response (shading) based on ten CMIP5 models  
 855 listed in Table 1: (a) the MME forced response, where gray dots and black dots indicate the  
 856 regions that at least seven and nine out of ten models agree on the sign of MME change, (b) the  
 857 uncertainty in the forced response (inter-model standard deviation of the projection), where dots  
 858 indicate the regions that the uncertainty is significantly larger than the internal climate  
 859 variability at the 90% confidence level of *F*-test, (c) the internal climate variability (intra-model  
 860 standard deviation of the projection), where dots indicate the regions where the internal climate  
 861 variability is significantly larger than the uncertainty at the 90% confidence level of *F*-test. Unit:  
 862 hPa.



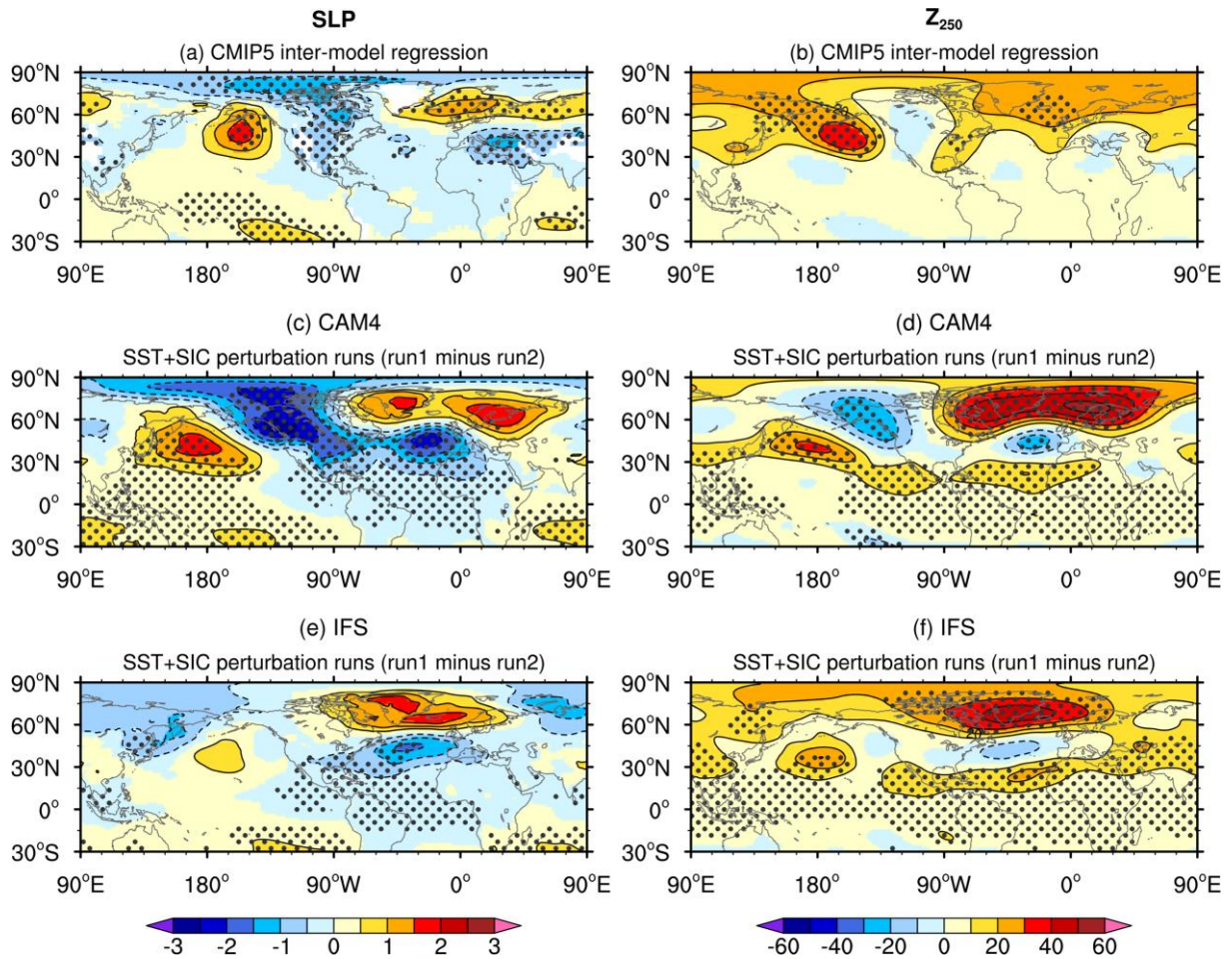
864

865 Fig. 2. (a)–(b) First two eigenvectors (EOF1 and EOF2; shading) and the uncertainty (inter-  
 866 model standard deviation; contour) in the forced DJF SLP response of the ten CMIP5 models,  
 867 (c) As in (a)–(b), but for the sum of EOF1 and EOF2, which is called the Pacific–Atlantic SLP  
 868 uncertainty pattern ( $PA_{\Delta SLP}$ ), (d) the inter-model relationship between the forced SLP response  
 869 over the northeastern Atlantic (60°–85°N and 20°W–10°E) and over the northeastern Pacific  
 870 (40°–65°N and 160°–135°W), where these regions are represented by the black boxes in (a)–  
 871 (c). Unit: hPa.



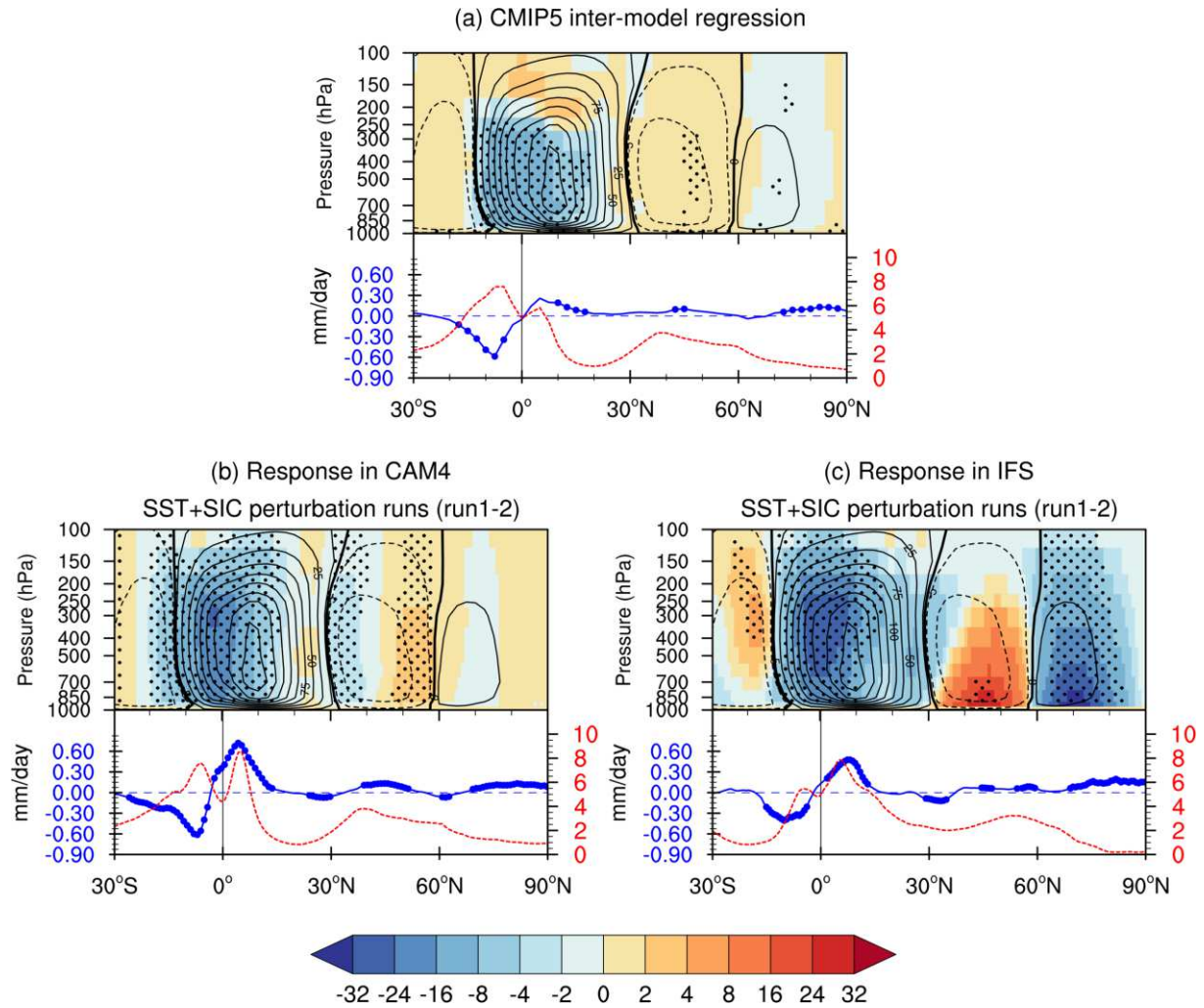
872

873 Fig. 3. (a)–(b) Inter-model regression of the forced response against  $PAI_{\Delta SL P}$  (shading) and the  
 874 uncertainty in the forced response (i.e., inter-model standard deviation; contour) of the ten  
 875 CMIP5 models: (a) SST (contour interval:  $0.4^{\circ}\text{C}$ ), (b) SIC (contour interval: 0.1 fraction), where  
 876 the outermost circle in the polar stereographic map is  $45^{\circ}\text{N}$ . (c)–(e) Scatterplot of the inter-  
 877 model relationship between  $PAI_{\Delta SL P}$  (abscissa) and the future projection (ordinate): (c) the  
 878 equator-to-pole SST gradient, (d) the inter-hemispheric SST gradient, (e) the zonal SST gradient  
 879 between the equatorial western and eastern Pacific ( $^{\circ}\text{C}$ ), and (f) the total Arctic sea ice extent  
 880 ( $10^6 \text{ km}^2$ ).



881

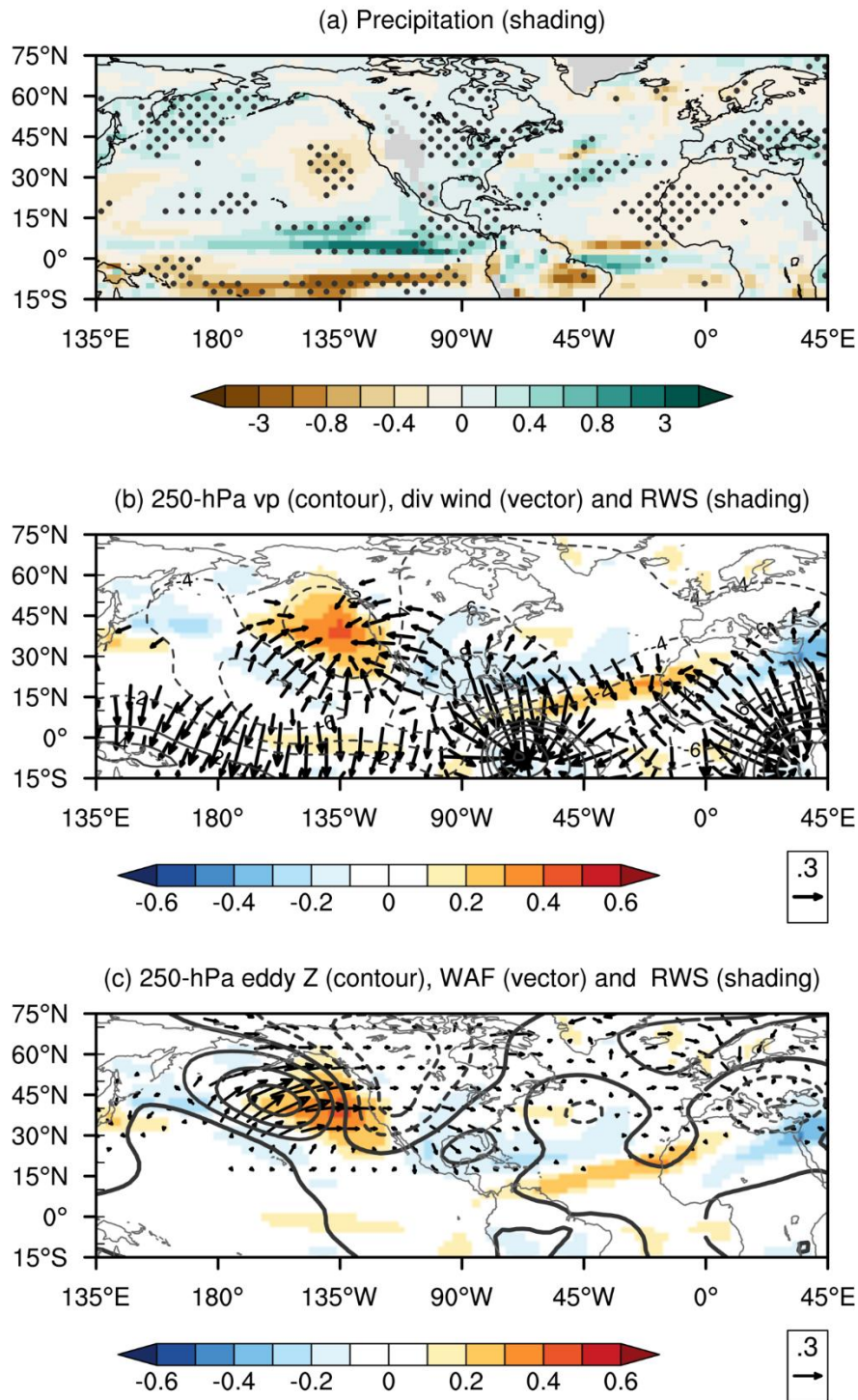
882 Fig. 4. Assessing the uncertainty in the DJF forced response of (left) SLP (contour interval: 0.5  
 883 hPa) and (right) 250-hPa geopotential height (contour interval: 10 m) associated with  $PA_{\Delta SLP}$ .  
 884 (a)–(b) Inter-model regression of the forced response against  $PAI_{\Delta SLP}$  across the ten CMIP5  
 885 models. (c)–(f) the AGCM response in the SST+SIC perturbation runs (run1 minus run2): (c)–  
 886 (d) CAM4, (e)–(f) IFS. Unit: hPa. Stippling indicates the 90% confidence level in the CMIP5  
 887 inter-model regression, and the 95% confidence level in AGCM experiments based on the two-  
 888 tailed Student's  $t$ -test.



889

890 Fig. 5. Assessing the uncertainty in the DJF forced response of the zonal-mean mass  
 891 streamfunction ( $10^9 \text{ kg s}^{-1}$ ) and the zonal-mean precipitation ( $\text{mm day}^{-1}$ ) associated with  $\text{PA}_{\Delta\text{SLP}}$ .  
 892 (a) Inter-model regression of the forced response against  $\text{PAI}_{\Delta\text{SLP}}$  across the ten CMIP5 models,  
 893 (b)–(c) the AGCM response in the SST+SIC perturbation runs (run1 minus run2): (b) CAM4,  
 894 and (c) IFS. For figures showing the zonal-mean mass streamfunction, the contour lines indicate  
 895 the 2069/70–2098/99 DJF climatology in the RCP8.5 scenario, where the thick lines indicate  
 896 0, the solid and dashed lines indicate the contours  $\pm 5 \times 10^9 \text{ kg s}^{-1}$  and the multiples of  $\pm 25 \times 10^9$   
 897  $\text{kg s}^{-1}$ . For figures showing the zonal-mean precipitation, blue line indicates the CMIP5 inter-  
 898 model regression or the AGCM response, and red line indicates the 2069/70–2098/99 DJF  
 899 climatology. Stippling and blue dots denotes the grid points exceeding the 95% confidence  
 900 interval of the zonal-mean mass streamfunction and the zonal-mean precipitation, respectively.

CMIP5 inter-model regression



901

902 Fig. 6. Inter-model regression of the forced response against  $PAI_{\Delta SLP}$  across the ten CMIP5  
 903 models. (a) Precipitation (shading;  $\text{mm day}^{-1}$ ). (b) 250-hPa velocity potential (contour;  $10^5 \text{ m}^2$   
 904  $\text{s}^{-1}$ ), divergent wind (vector;  $\text{m s}^{-1}$ ), and Rossby wave source (shading;  $10^{-11} \text{ s}^{-2}$ ). (c) 250-hPa  
 905 eddy geopotential height (contour interval: 10 m) and horizontal component of wave activity  
 906 fluxes (vector;  $\text{m}^2 \text{ s}^{-2}$ ), and Rossby wave source (shading;  $10^{-11} \text{ s}^{-2}$ ) Stippling in (a) indicates  
 907 the 95% confidence level.

**Response in SST perturbation runs (run1-2)**

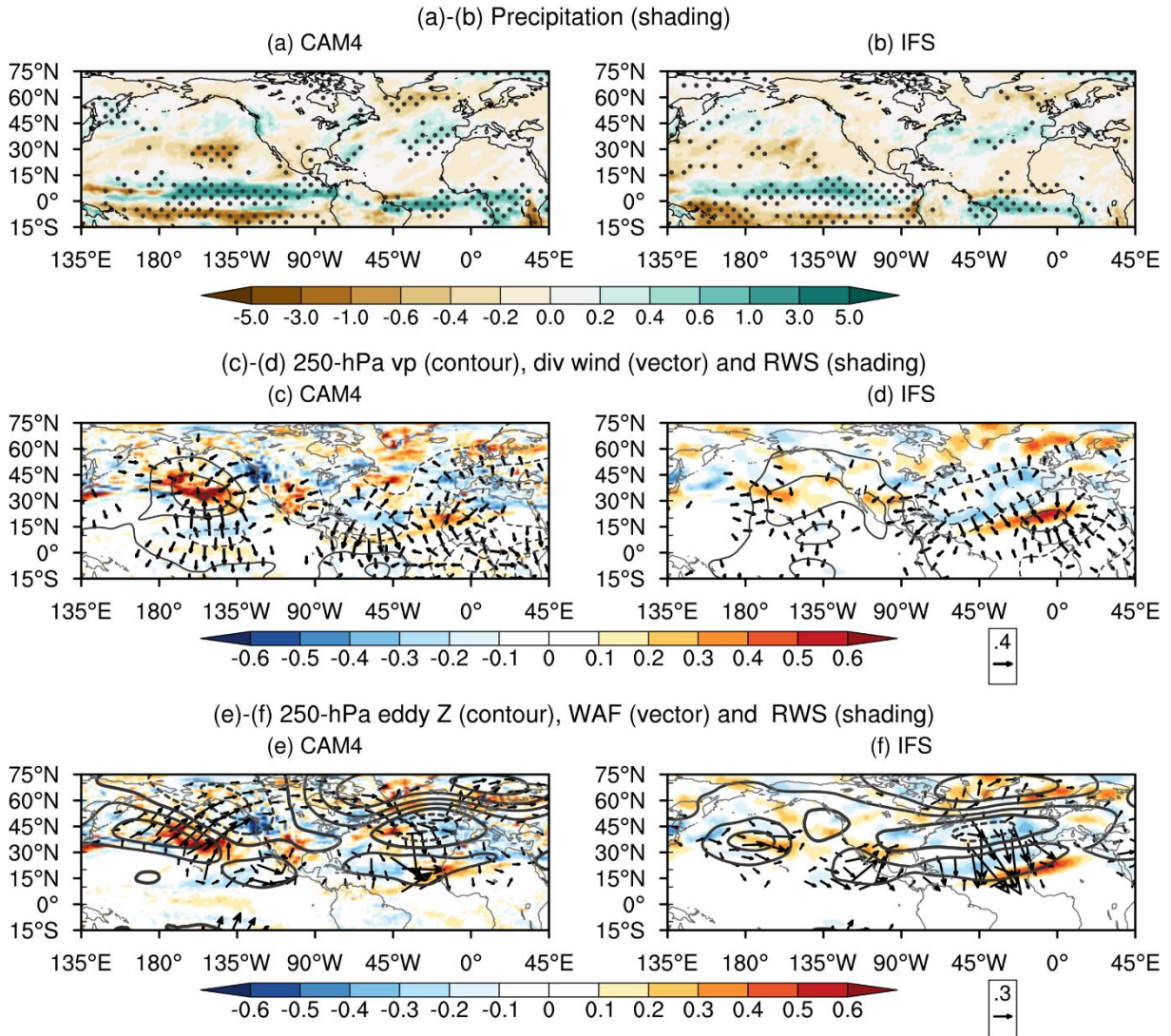
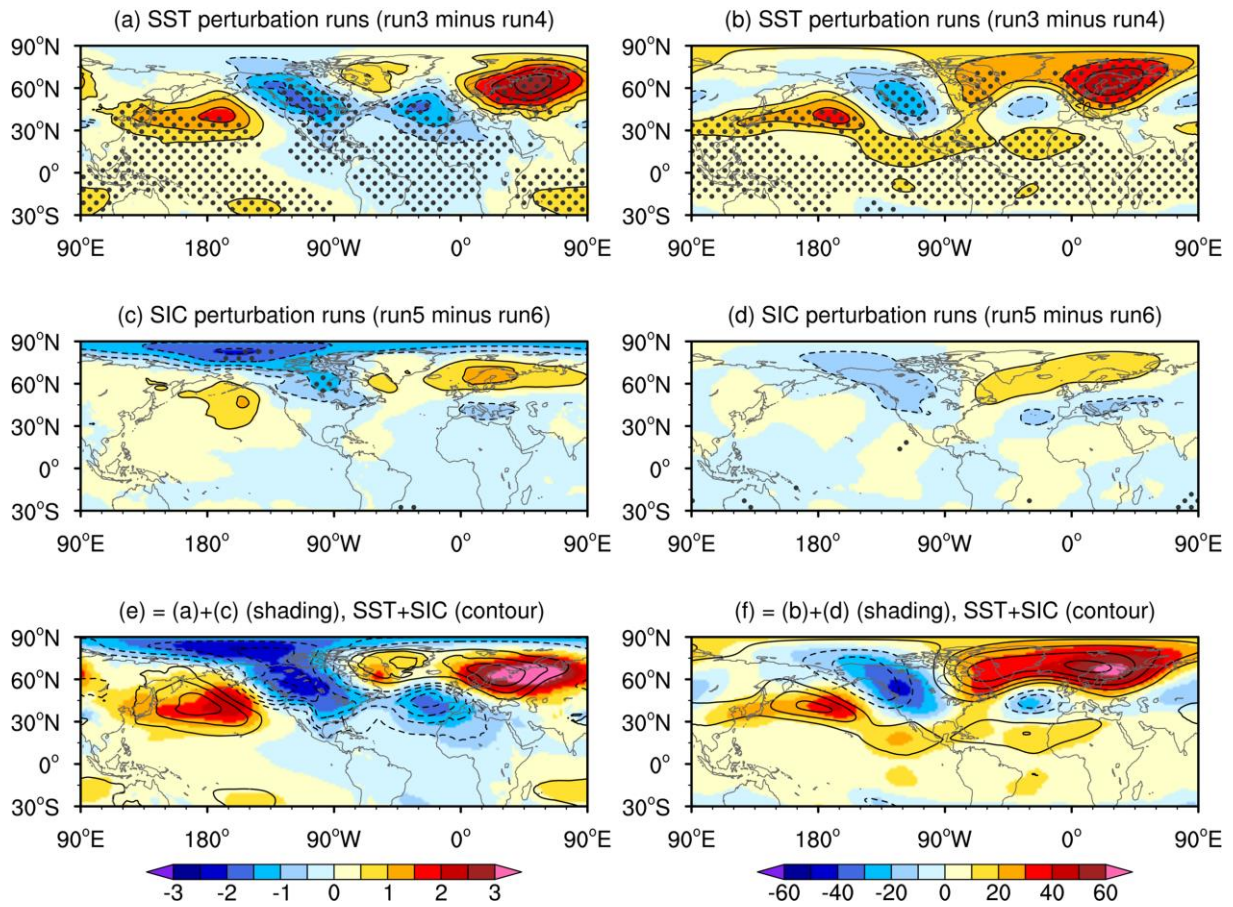


Fig. 7. As in Fig. 6, but for the (left) CAM4 and (right) IFS responses in the SST+SIC perturbation runs.

DJF response of SLP (left) and  $Z_{250}$  (right) in CAM4



912

913 Fig. 8. DJF response of (left) SLP (contour interval: 0.5 hPa) and (right) 250-hPa geopotential  
 914 height (contour interval: 10 m) in CAM4. (a)–(b) the SST perturbation runs, and (c)–(d) the  
 915 SIC perturbation runs, (e)–(f) the response in the SST+SIC perturbation runs (contour) and the  
 916 sum of responses in the SST perturbation runs and the SIC perturbation runs (shading). In (a)–  
 917 (d), stippling indicates the 95% confidence level based on the two-tailed Student's *t*-test.

DJF response of SLP (left) and  $Z_{250}$  (right) in IFS

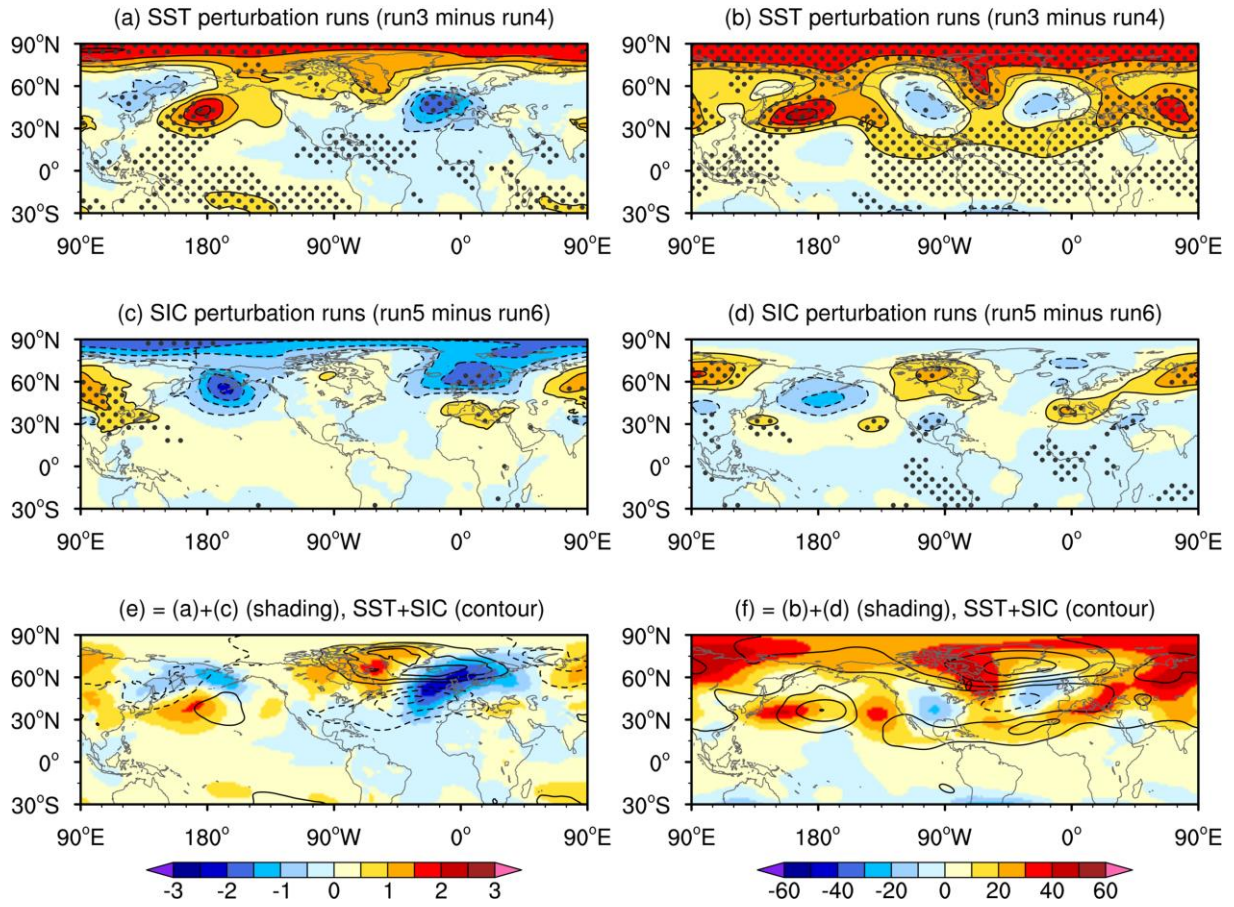
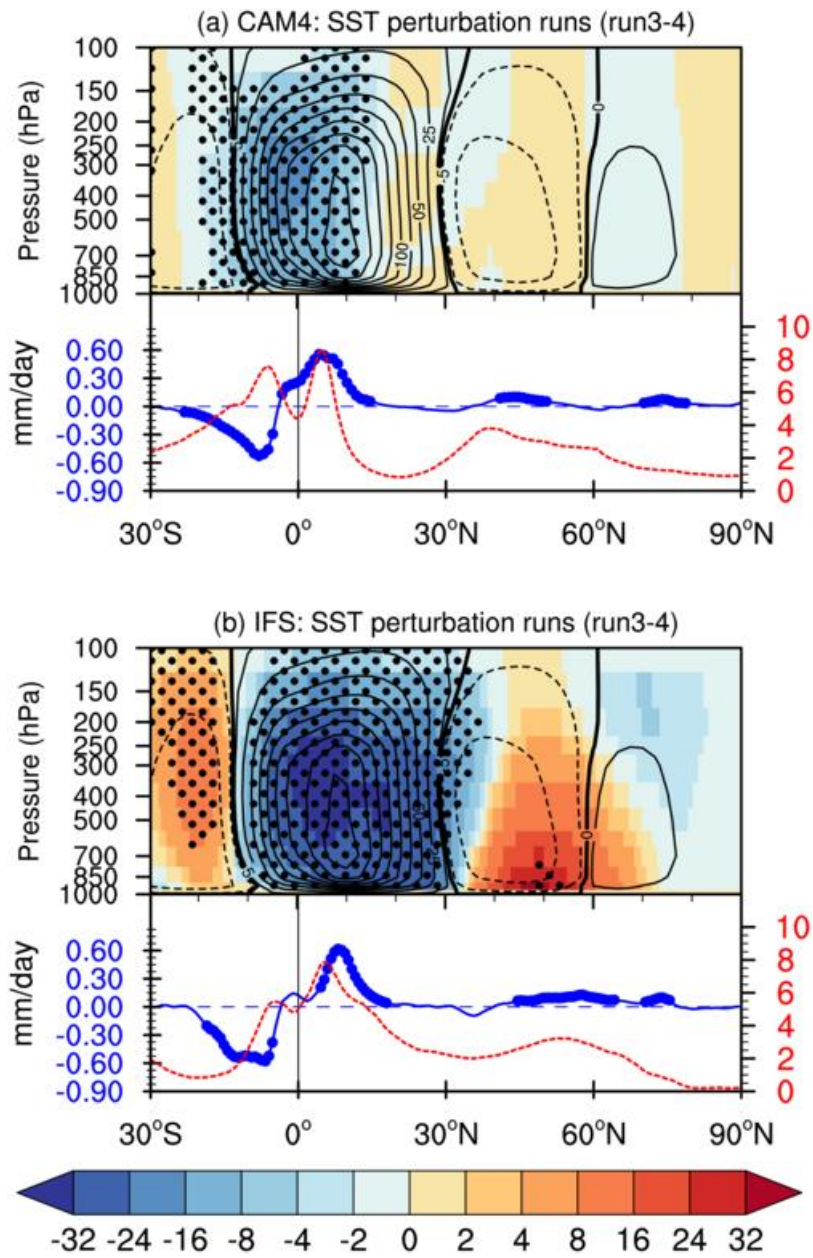


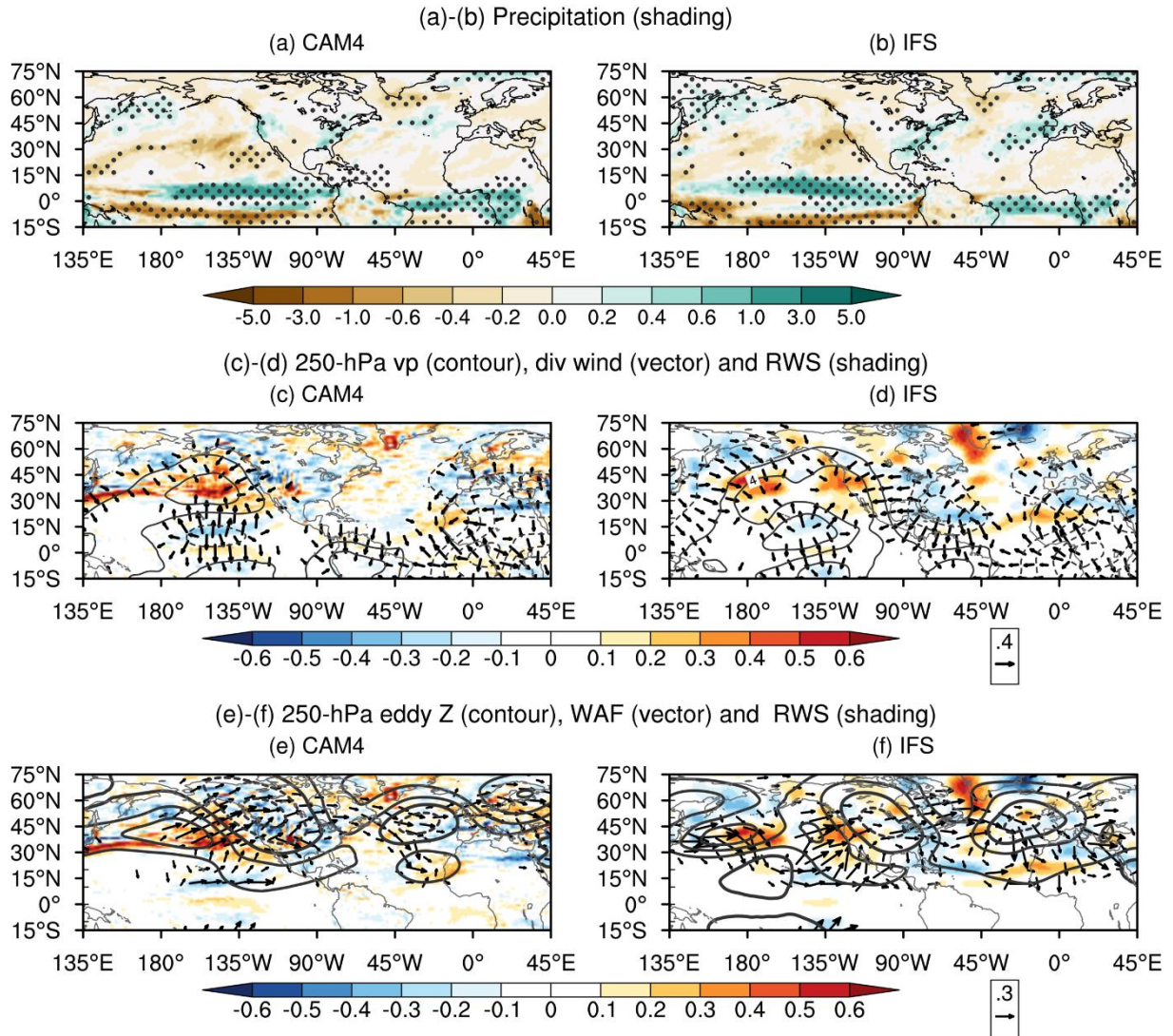
Fig. 9. As in Fig. 8, but for the response in IFS.



920

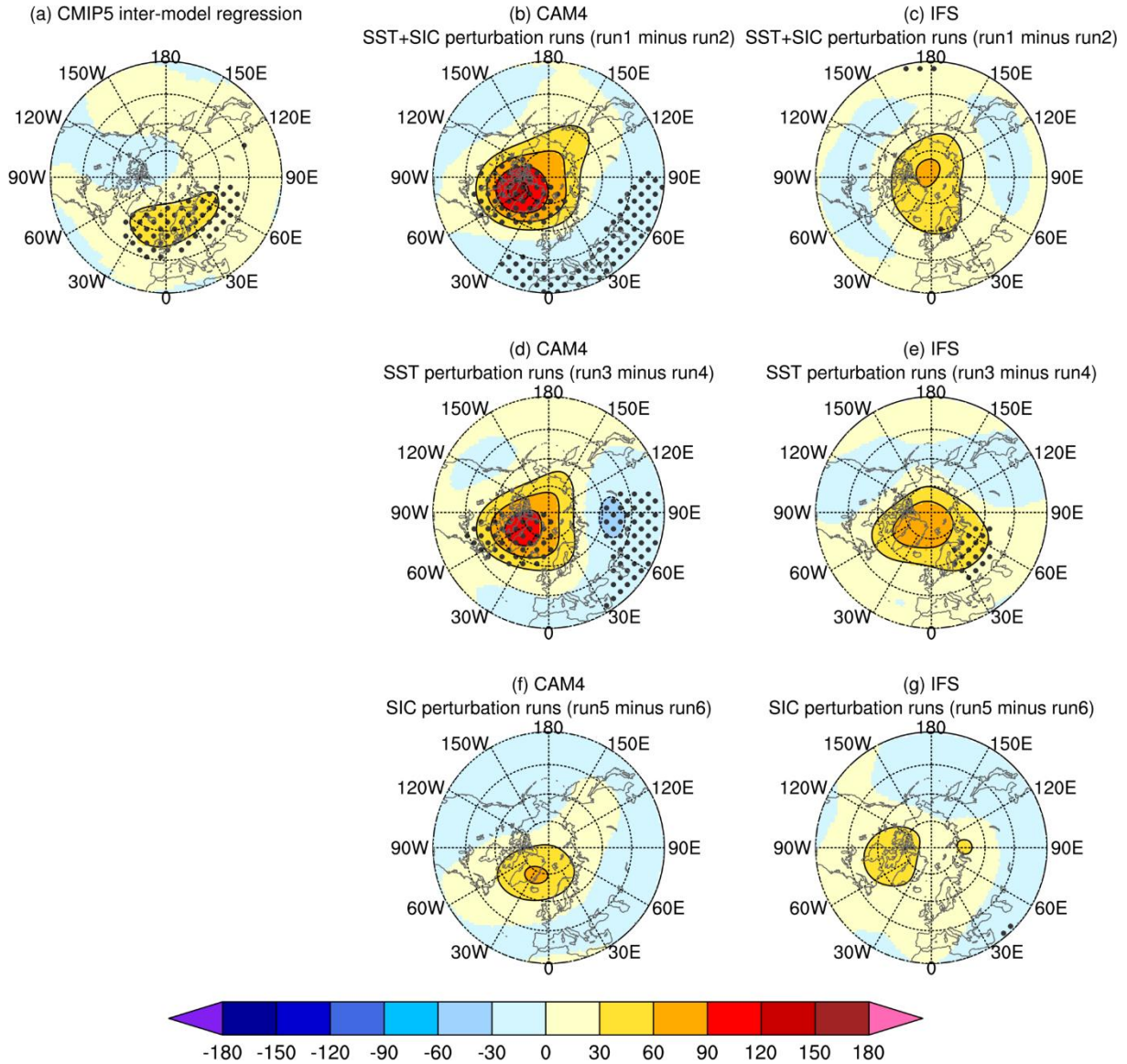
921 Fig. 10. As in Fig. 5, but for the response of CAM4 and IFS in the SST perturbation runs.

**Response in SST perturbation runs (run3-4)**



922

923 Fig. 11. As in Fig. 6, but for the response in the SST perturbation runs: (left) CAM4 and (right)  
 924 IFS.



927 Fig. 12. Assessing the uncertainty in the DJF response of the 10-hPa geopotential height  
 928 (contour interval: 30 m) associated with  $PA_{\Delta SL P}$ . (a) Inter-model regression of the forced  
 929 response against  $PA_{\Delta SL P}$  across the ten CMIP5 models. The response of (middle) CAM4 and  
 930 (right) IFS in (b)–(c) the SST+SIC perturbation runs (run1 minus run2), (d)–(e) the SST  
 931 perturbation runs (run3 minus run4), and (f)–(g) the SIC perturbation runs (run 5 minus run6).  
 932 Unit: hPa. Shading indicates the 90% confidence level in the CMIP5 inter-model regression,  
 933 and the 95% confidence level in AGCM experiments based on the two-tailed Student’s *t*-test.

# Figures

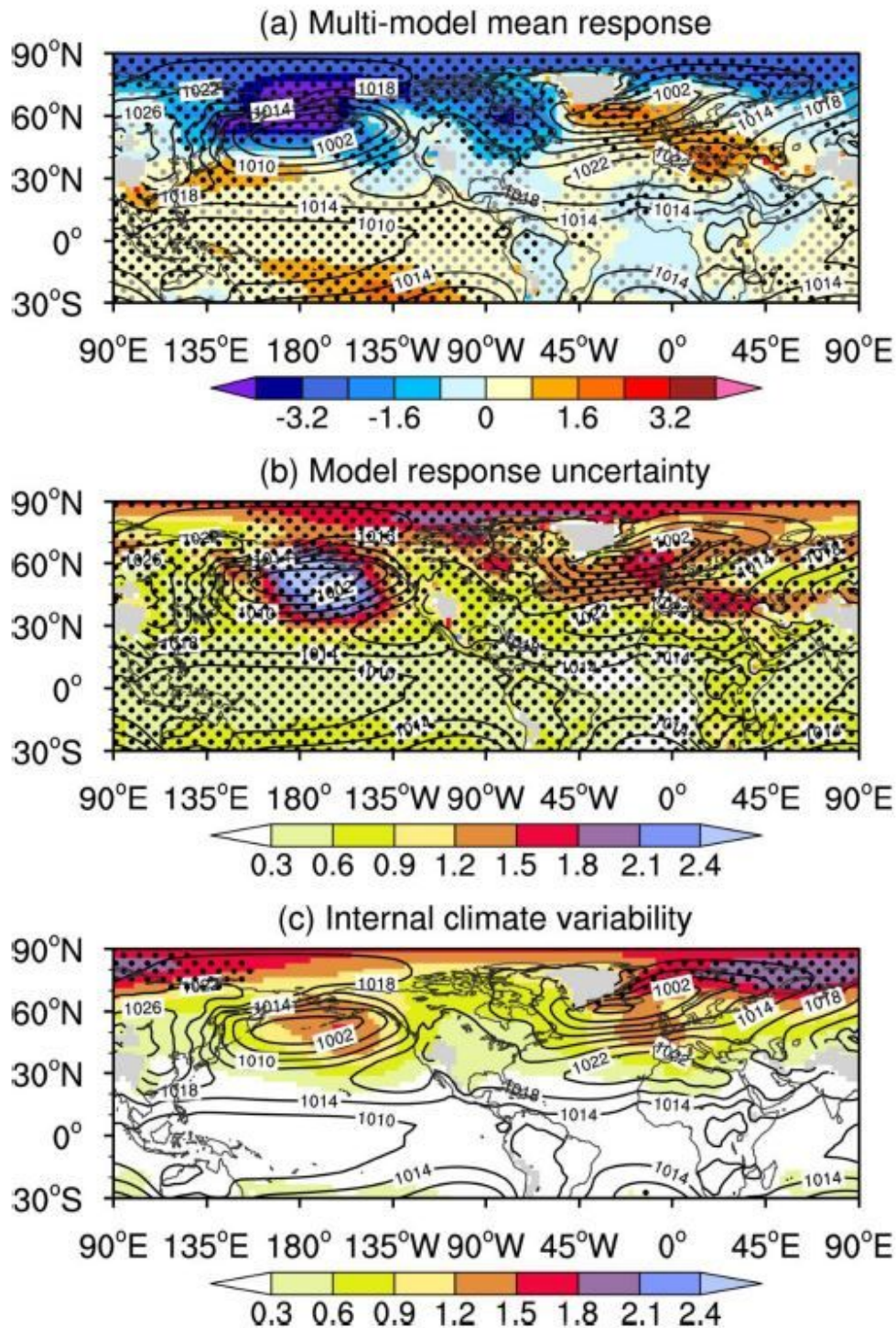
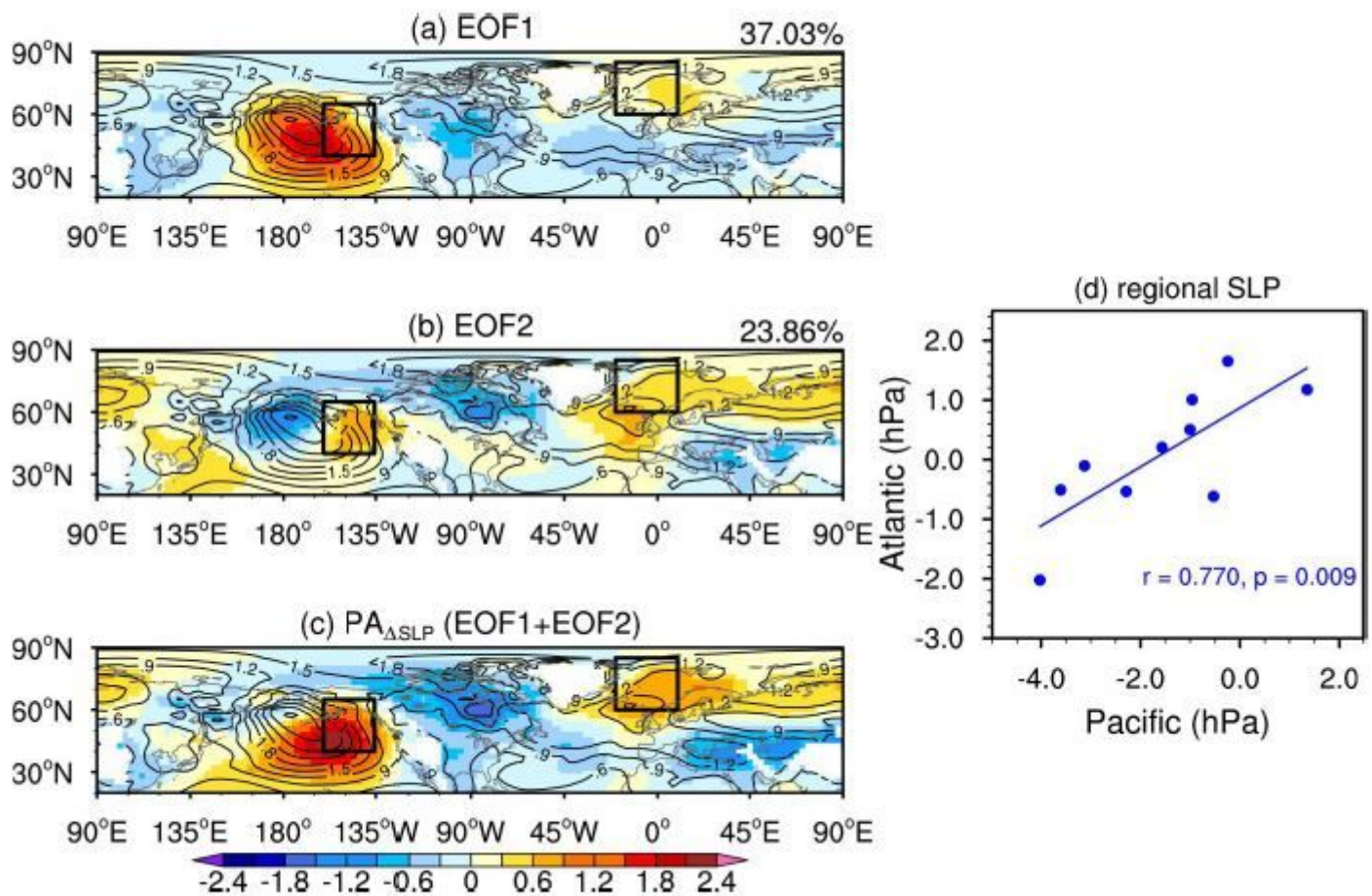


Figure 1

Multi-model mean (MME) of the DJF sea level pressure (SLP) in 1971/72–2000/01 of the historical run (contour), and the forced response (shading) based on ten CMIP5 models listed in Table 1: (a) the MME forced response, where gray dots and black dots indicate the regions that at least seven and nine out of

ten models agree on the sign of MME change, (b) the uncertainty in the forced response (inter-model standard deviation of the projection), where dots indicate the regions that the uncertainty is significantly larger than the internal climate variability at the 90% confidence level of F-test, (c) the internal climate variability (intra-model standard deviation of the projection), where dots indicate the regions where the internal climate variability is significantly larger than the uncertainty at the 90% confidence level of F-test. Unit: hPa. Note: The designations employed and the presentation of the material on this map do not imply the expression of any opinion whatsoever on the part of Research Square concerning the legal status of any country, territory, city or area or of its authorities, or concerning the delimitation of its frontiers or boundaries. This map has been provided by the authors.



**Figure 2**

(a)–(b) First two eigenvectors (EOF1 and EOF2; shading) and the uncertainty (inter-865 model standard deviation; contour) in the forced DJF SLP response of the ten CMIP5 models, 866 (c) As in (a)–(b), but for the sum of EOF1 and EOF2, which is called the Pacific–Atlantic SLP 867 uncertainty pattern (PA<sub>ΔSLP</sub>), (d) the inter-model relationship between the forced SLP response 868 over the northeastern Atlantic (60°–85°N and 20°W–10°E) and over the northeastern Pacific 869 (40°–65°N and 160°–135°W), where these regions are represented by the black boxes in (a)–870 (c). Unit: hPa. Note: The designations employed and the presentation of the material on this map do not imply the expression of any opinion whatsoever

on the part of Research Square concerning the legal status of any country, territory, city or area or of its authorities, or concerning the delimitation of its frontiers or boundaries. This map has been provided by the authors.

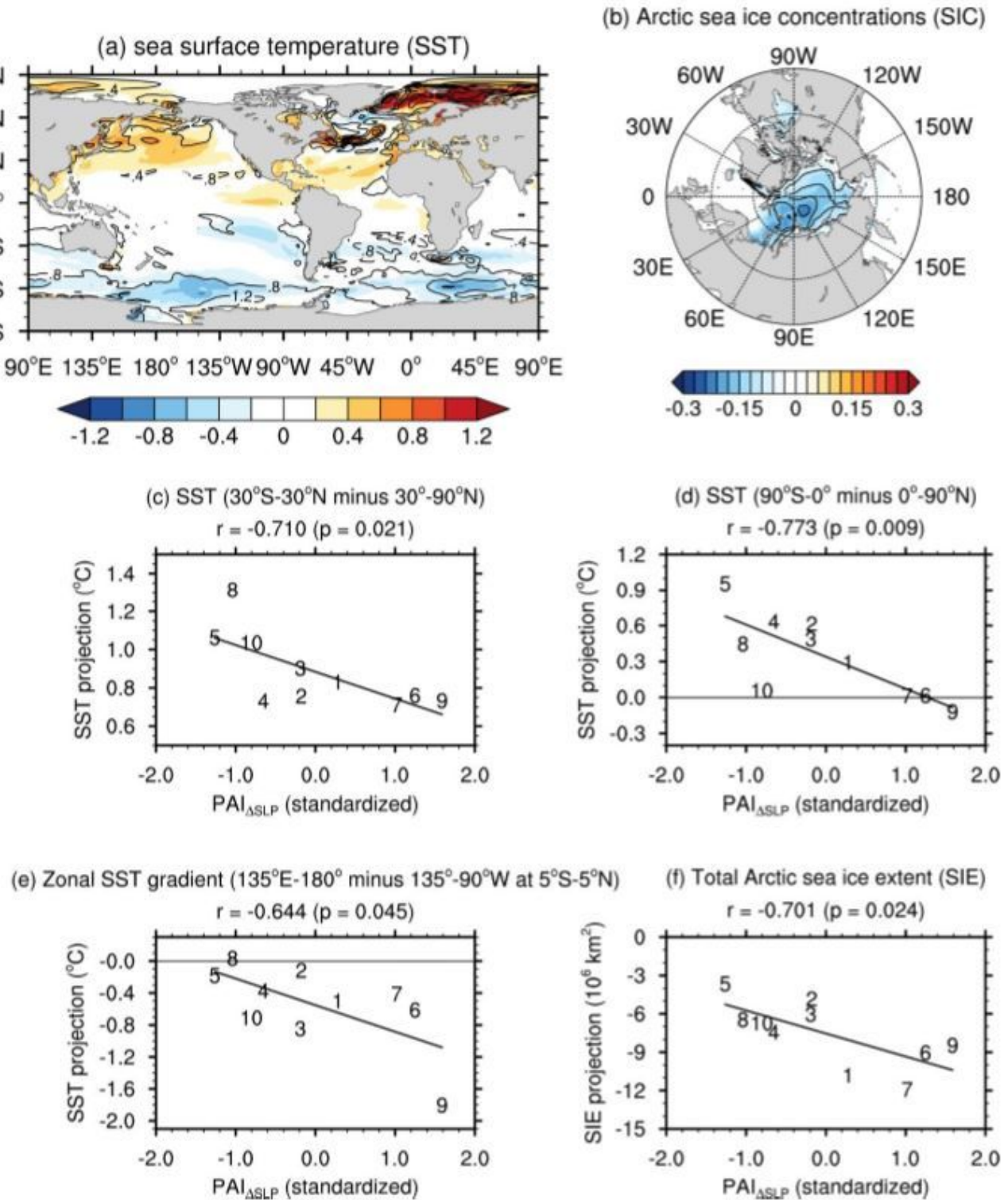


**Figure 3**

(a)–(b) Inter-model regression of the forced response against  $PAI_{\Delta SL P}$  (shading) and the 873 uncertainty in the forced response (i.e., inter-model standard deviation; contour) of the ten 874 CMIP5 models: (a)

SST (contour interval: 0.4°C), (b) SIC (contour interval: 0.1 fraction), where 875 the outermost circle in the polar stereographic map is 45°N. (c)–(e) Scatterplot of the inter-876 model relationship between  $\text{PAI}\Delta\text{SLP}$  (abscissa) and the future projection (ordinate): (c) the 877 equator-to-pole SST gradient, (d) the inter-hemispheric SST gradient, (e) the zonal SST gradient 878 between the equatorial western and eastern Pacific (°C), and (f) the total Arctic sea ice extent 879 (106 km<sup>2</sup>). Note: The designations employed and the presentation of the material on this map do not imply the expression of any opinion whatsoever on the part of Research Square concerning the legal status of any country, territory, city or area or of its authorities, or concerning the delimitation of its frontiers or boundaries. This map has been provided by the authors.

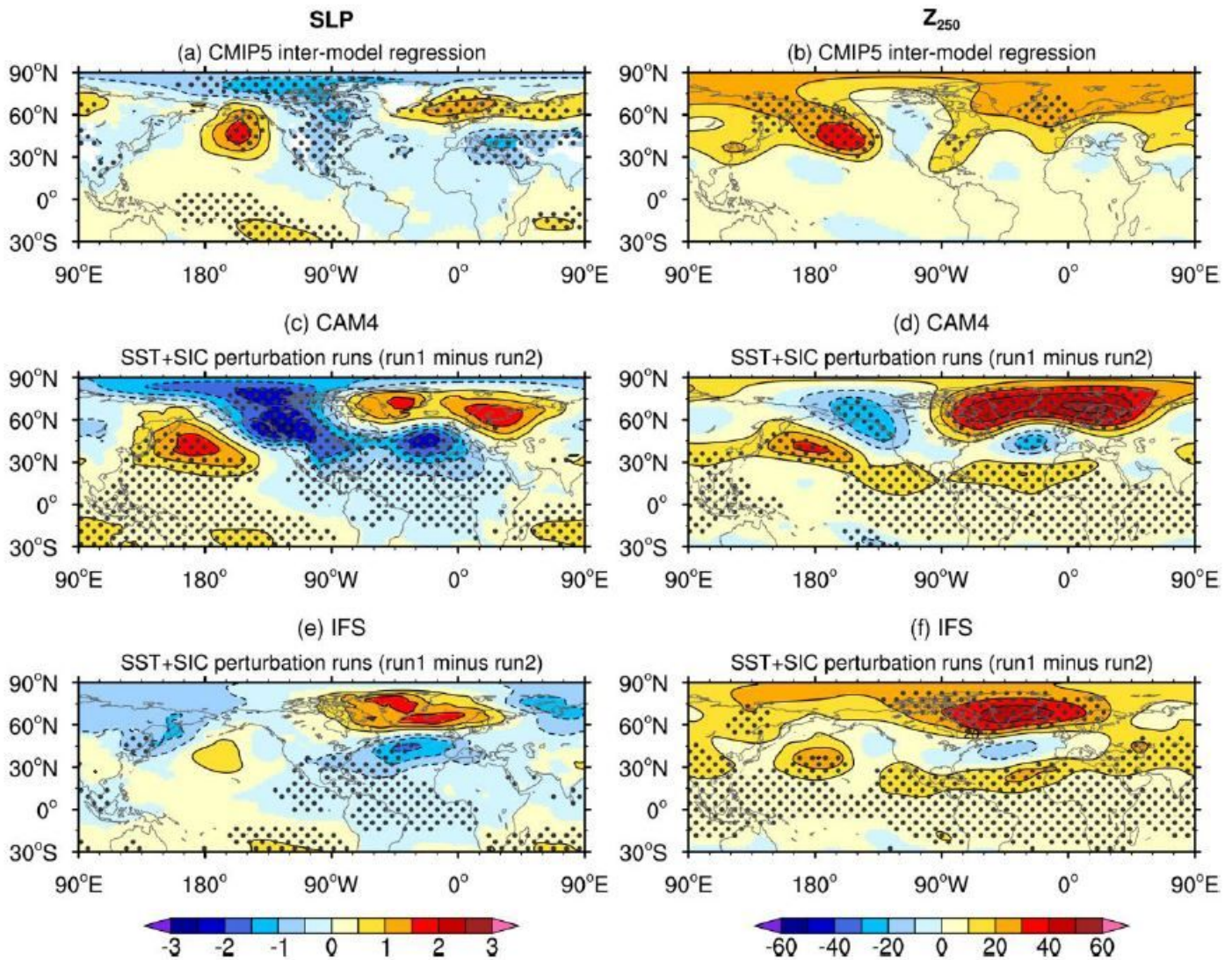


**Figure 4**

Assessing the uncertainty in the DJF forced response of (left) SLP (contour interval: 0.5 882 hPa) and (right) 250-hPa geopotential height (contour interval: 10 m) associated with  $\text{PA}\Delta\text{SLP}$ . 883 (a)–(b) Inter-model regression of the forced response against  $\text{PA}\Delta\text{SLP}$  across the ten CMIP5 884 models. (c)–(f) the

AGCM response in the SST+SIC perturbation runs (run1 minus run2): (c)–885 (d) CAM4, (e)–(f) IFS. Unit: hPa. Stippling indicates the 90% confidence level in the CMIP5 886 inter-model regression, and the 95% confidence level in AGCM experiments based on the two-887 tailed Student’s t-test. Note: The designations employed and the presentation of the material on this map do not imply the expression of any opinion whatsoever on the part of Research Square concerning the legal status of any country, territory, city or area or of its authorities, or concerning the delimitation of its frontiers or boundaries. This map has been provided by the authors.

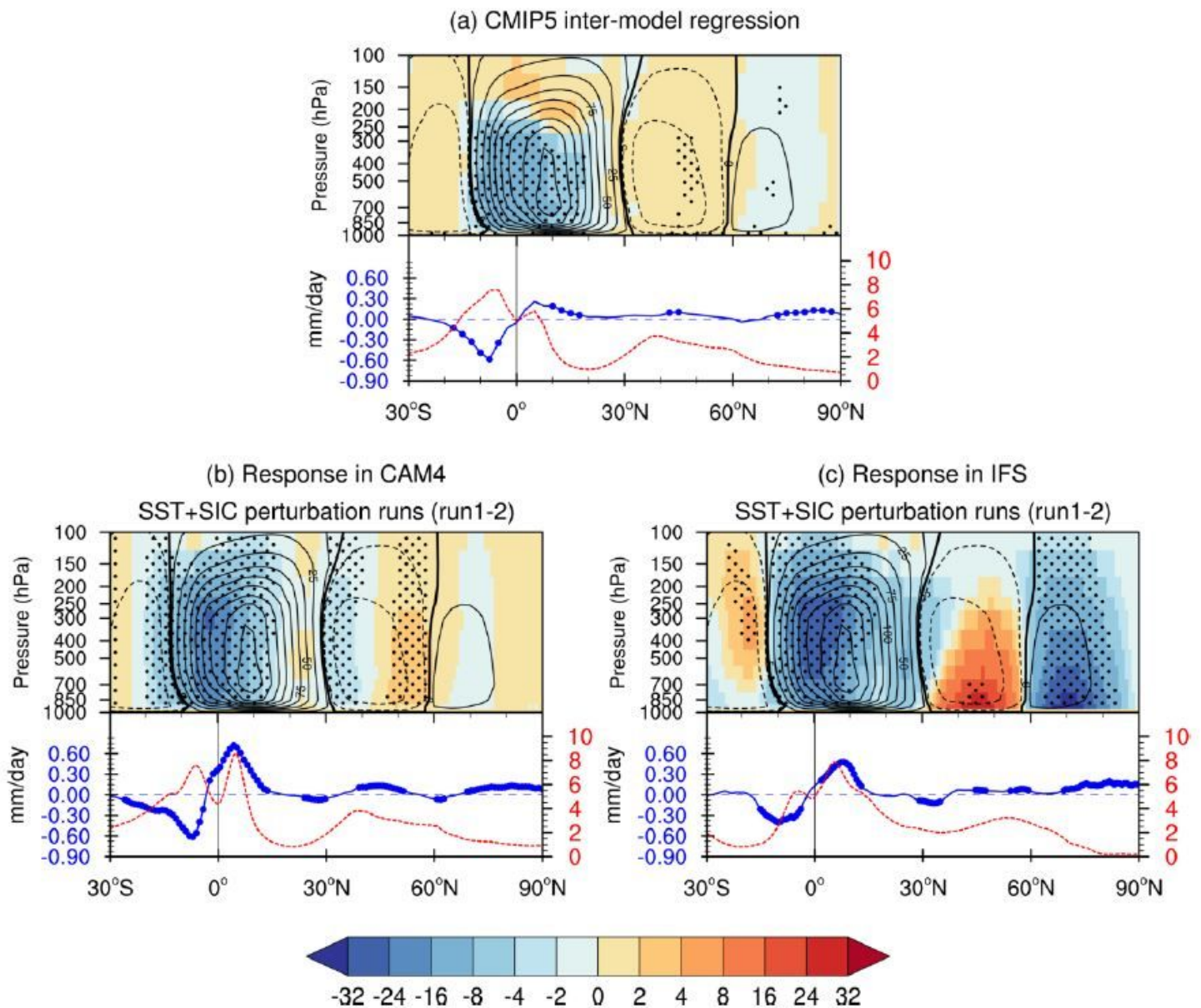


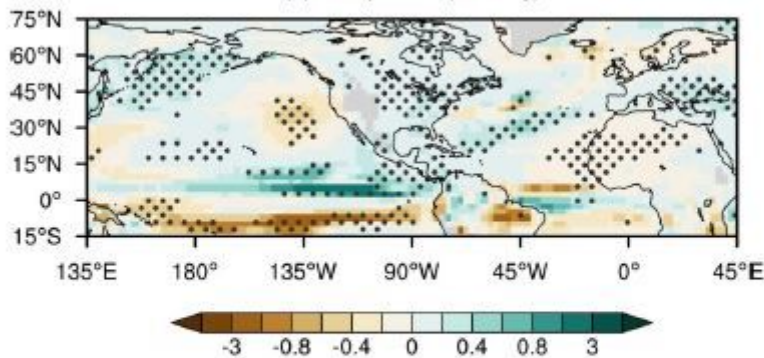
**Figure 5**

Assessing the uncertainty in the DJF forced response of the zonal-mean mass 890 streamfunction ( $10^9 \text{ kg s}^{-1}$ ) and the zonal-mean precipitation ( $\text{mm day}^{-1}$ ) associated with PA $\Delta$ SLP. 891 (a) Inter-model regression of the forced response against PA $\Delta$ SLP across the ten CMIP5 models, 892 (b)–(c) the AGCM

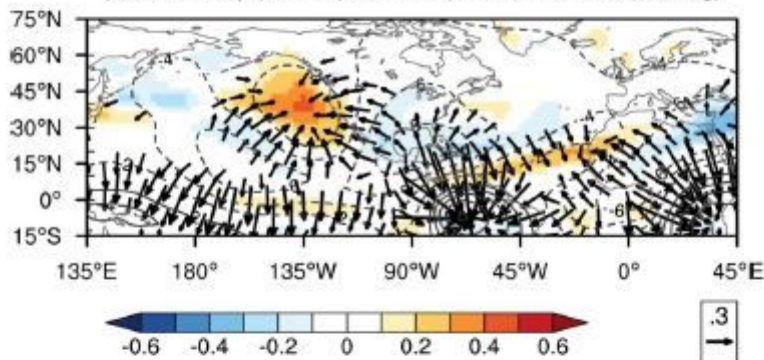
response in the SST+SIC perturbation runs (run1 minus run2): (b) CAM4, 893 and (c) IFS. For figures showing the zonal-mean mass streamfunction, the contour lines indicate 894 the 2069/70–2098/99 DJF climatology in the RCP8.5 scenario, where the thick lines indicate 895 0, the solid and dashed lines indicate the contours  $\pm 5 \times 10^9 \text{ kg s}^{-1}$  and the multiples of  $\pm 25 \times 10^9 \text{ kg s}^{-1}$ . For figures showing the zonal-mean precipitation, blue line indicates the CMIP5 inter-897 model regression or the AGCM response, and red line indicates the 2069/70–2098/99 DJF 898 climatology. Stippling and blue dots denotes the grid points exceeding the 95% confidence 899 interval of the zonal-mean mass streamfunction and the zonal-mean precipitation, respectively. Note: The designations employed and the presentation of the material on this map do not imply the expression of any opinion whatsoever on the part of Research Square concerning the legal status of any country, territory, city or area or of its authorities, or concerning the delimitation of its frontiers or boundaries. This map has been provided by the authors.

CMIP5 inter-model regression

(a) Precipitation (shading)



(b) 250-hPa vp (contour), div wind (vector) and RWS (shading)



(c) 250-hPa eddy Z (contour), WAF (vector) and RWS (shading)

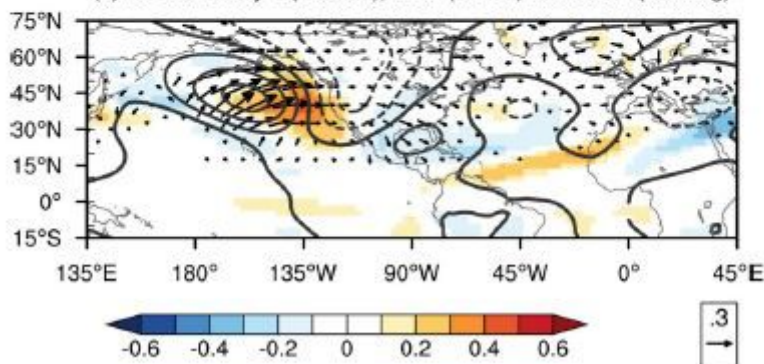


**Figure 6**

Inter-model regression of the forced response against  $\text{PAI}\Delta\text{SLP}$  across the ten CMIP5 902 models. (a) Precipitation (shading;  $\text{mm day}^{-1}$ ). (b) 250-hPa velocity potential (contour;  $10^5 \text{ m}^2 \text{ 90}^3 \text{ s}^{-1}$ ), divergent wind (vector;  $\text{m s}^{-1}$ ), and Rossby wave source (shading;  $10^{-11} \text{ s}^{-2}$ ). (c) 250-hPa 904 eddy geopotential height (contour interval: 10 m) and horizontal component of wave activity 905 fluxes (vector;  $\text{m}^2 \text{ s}^{-2}$ ), and Rossby wave source (shading;  $10^{-11} \text{ s}^{-2}$ ) Stippling in (a) indicates 906 the 95% confidence level. Note: The designations employed and the presentation of the material on this map do not imply the expression of any opinion whatsoever on the part of Research Square concerning the legal status of any country, territory, city or area or of its authorities, or concerning the delimitation of its frontiers or boundaries. This map has been provided by the authors.

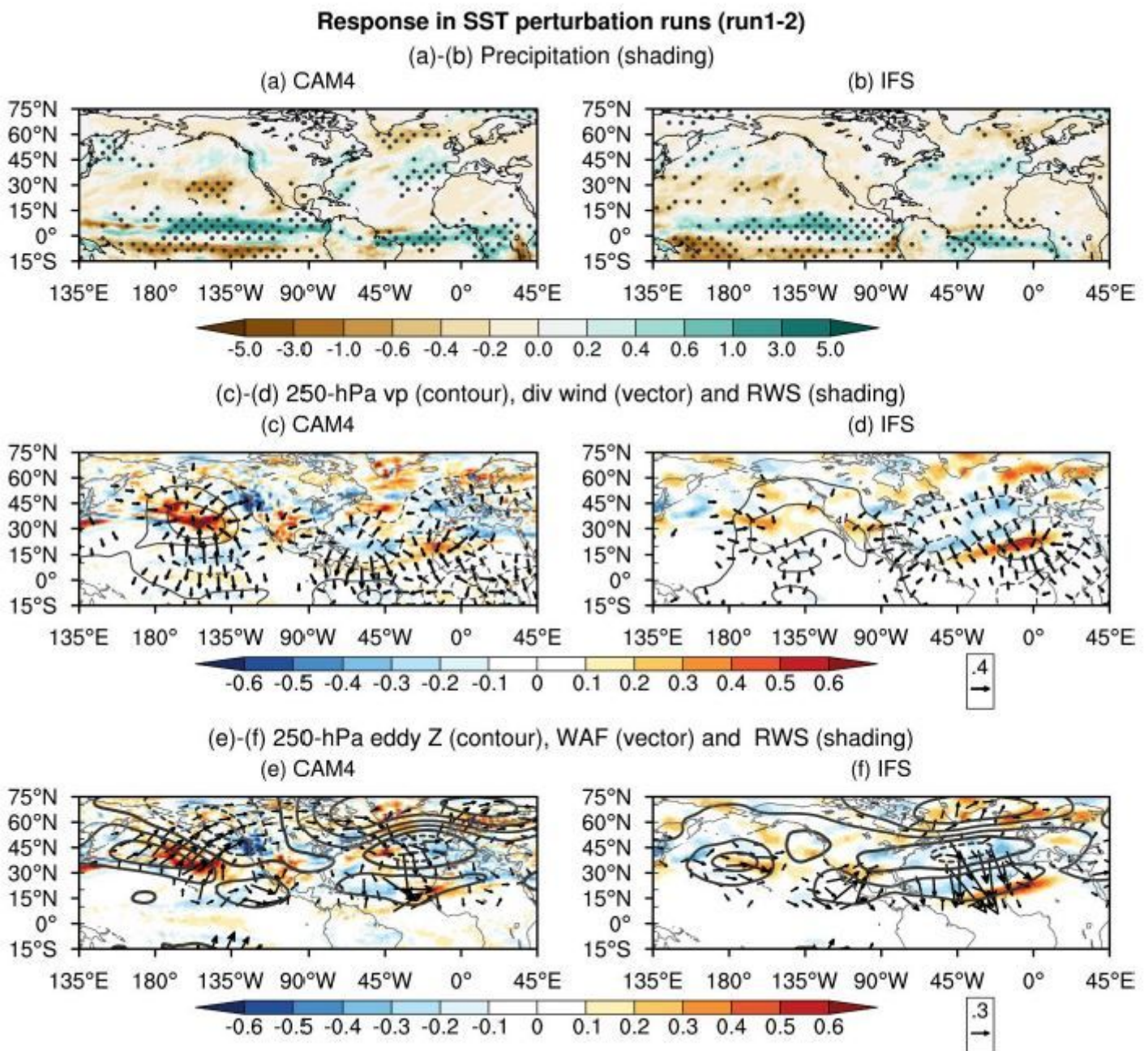


## Figure 7

As in Fig. 6, but for the (left) CAM4 and (right) IFS responses in the SST+SIC perturbation runs. Note: The designations employed and the presentation of the material on this map do not imply the expression of any opinion whatsoever on the part of Research Square concerning the legal status of any country, territory, city or area or of its authorities, or concerning the delimitation of its frontiers or boundaries. This map has been provided by the authors.

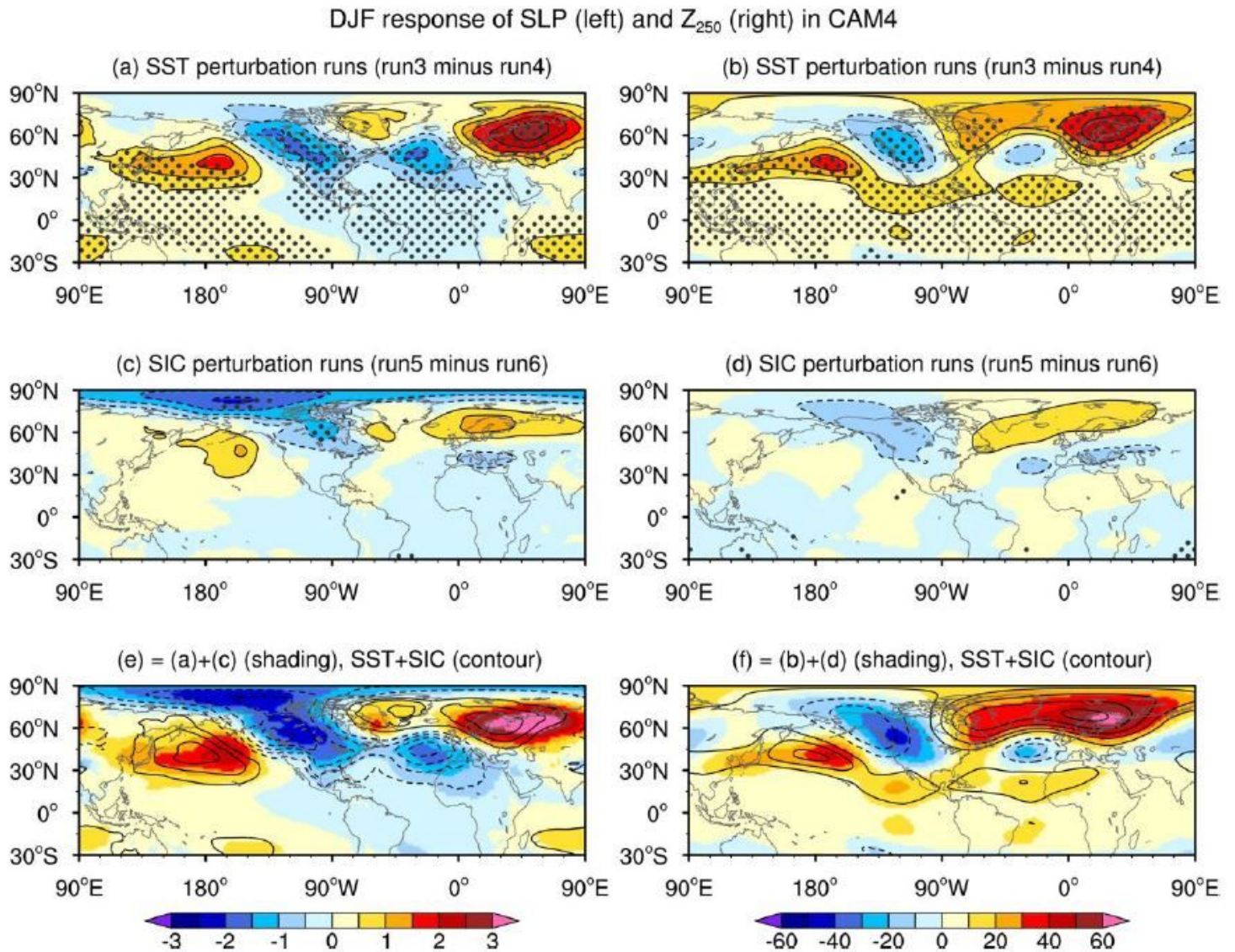


## Figure 8

DJF response of (left) SLP (contour interval: 0.5 hPa) and (right) 250-hPa geopotential height (contour interval: 10 m) in CAM4. (a)–(b) the SST perturbation runs, and (c)–(d) the SIC perturbation runs, (e)–(f) the response in the SST+SIC perturbation runs (contour) and the sum of responses in the SST perturbation runs and the SIC perturbation runs (shading). In (a)–(d), stippling indicates the 95% confidence level based on the two-tailed Student's t-test. Note: The designations employed and the

presentation of the material on this map do not imply the expression of any opinion whatsoever on the part of Research Square concerning the legal status of any country, territory, city or area or of its authorities, or concerning the delimitation of its frontiers or boundaries. This map has been provided by the authors.

DJF response of SLP (left) and  $Z_{250}$  (right) in IFS

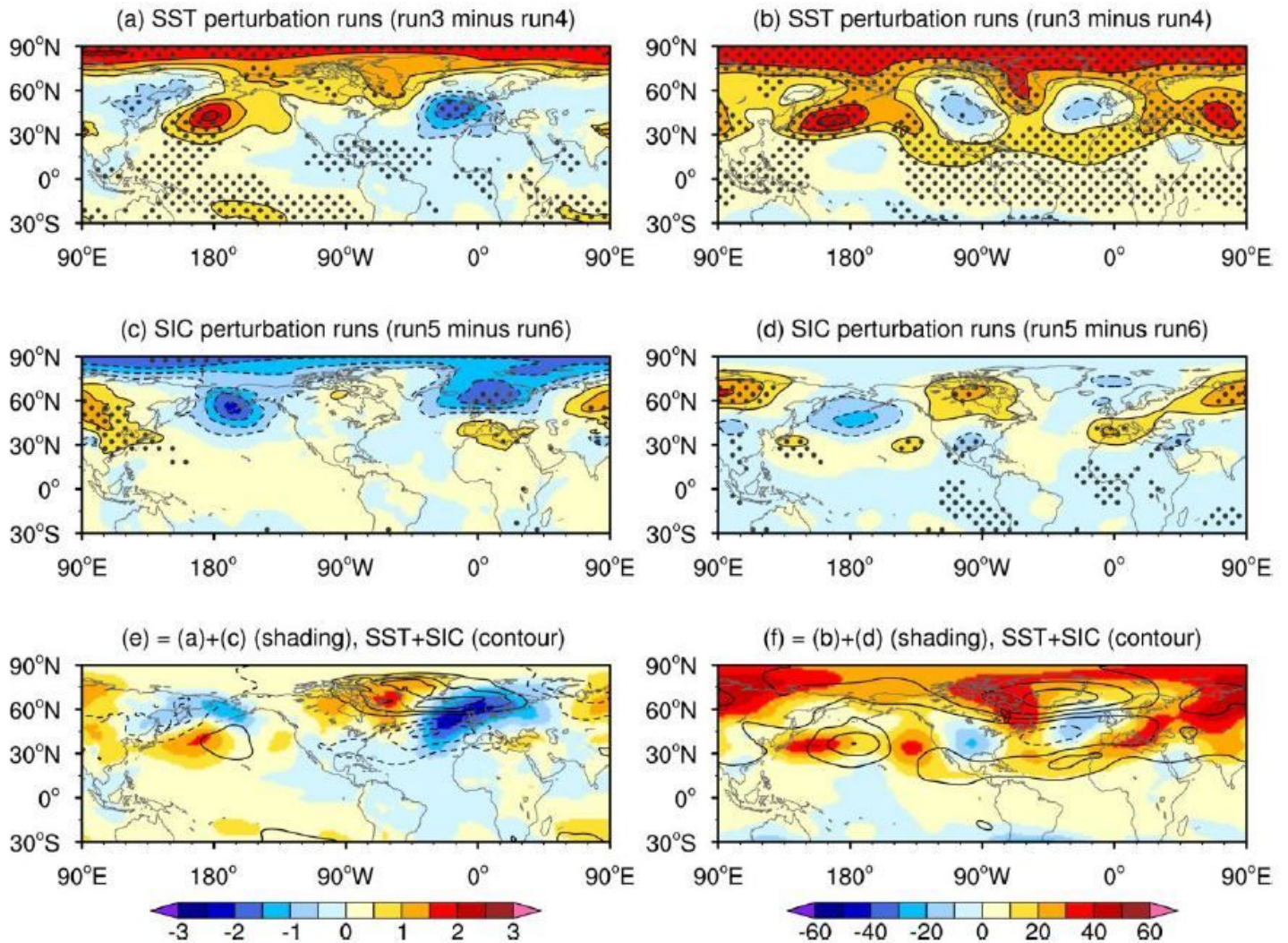


**Figure 9**

As in Fig. 8, but for the response in IFS. Note: The designations employed and the presentation of the material on this map do not imply the expression of any opinion whatsoever on the part of Research Square concerning the legal status of any country, territory, city or area or of its authorities, or concerning the delimitation of its frontiers or boundaries. This map has been provided by the authors.

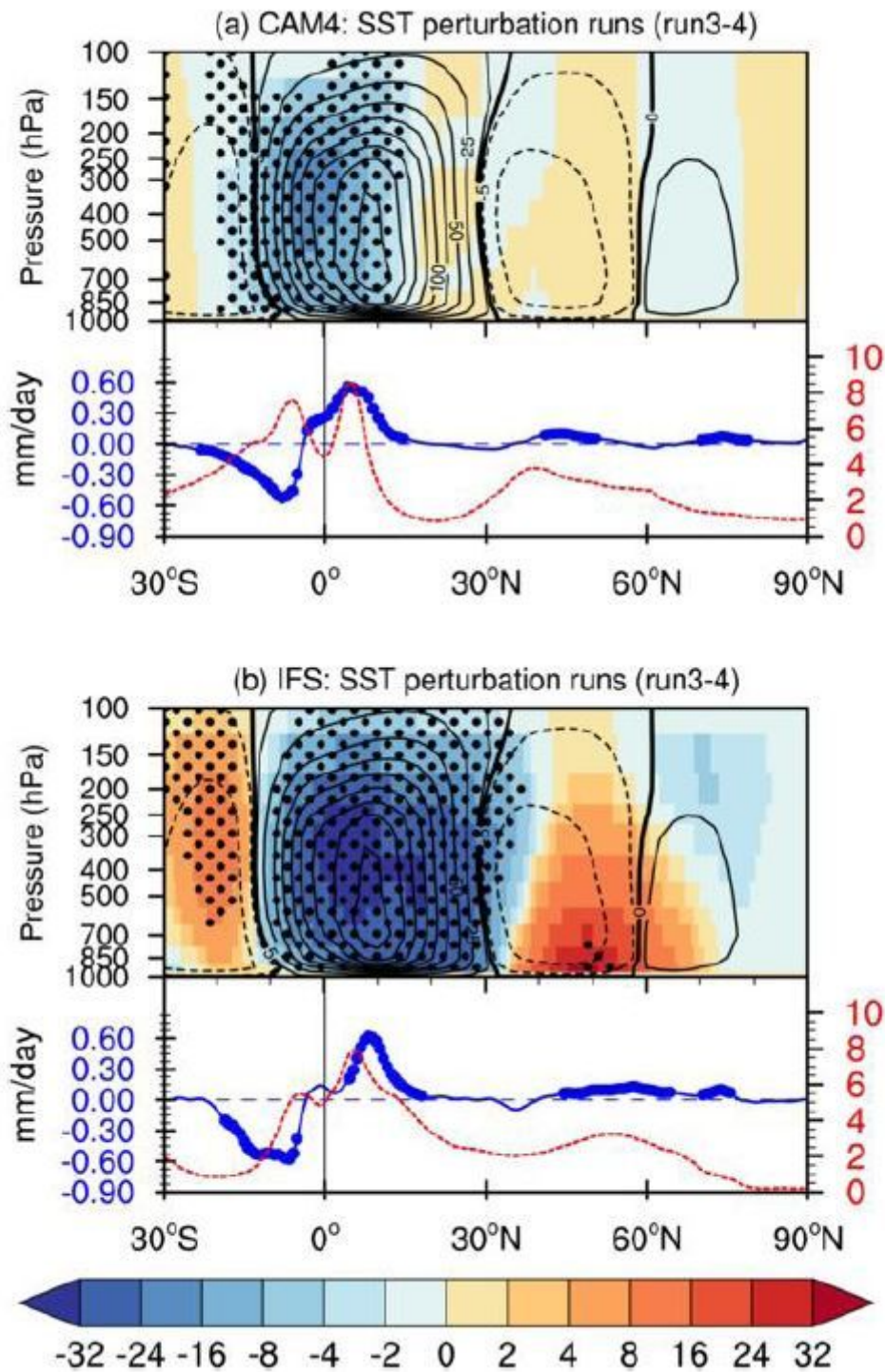


**Figure 10**

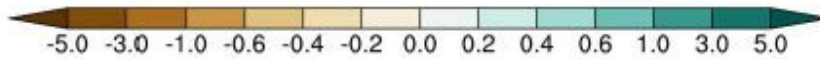
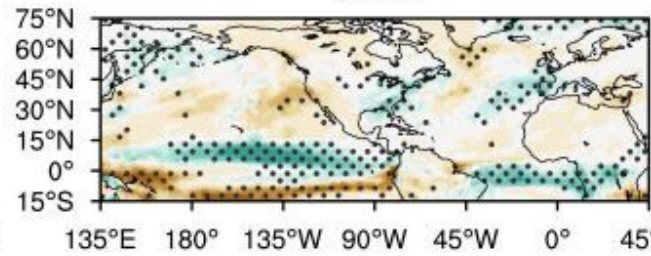
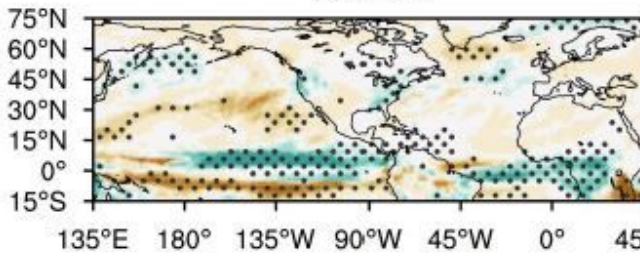
As in Fig. 5, but for the response of CAM4 and IFS in the SST perturbation runs. Note: The designations employed and the presentation of the material on this map do not imply the expression of any opinion whatsoever on the part of Research Square concerning the legal status of any country, territory, city or area or of its authorities, or concerning the delimitation of its frontiers or boundaries. This map has been provided by the authors.

### Response in SST perturbation runs (run3-4)

(a)-(b) Precipitation (shading)

(a) CAM4

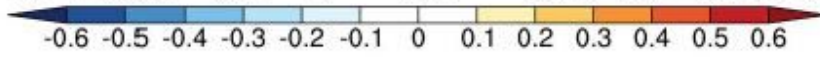
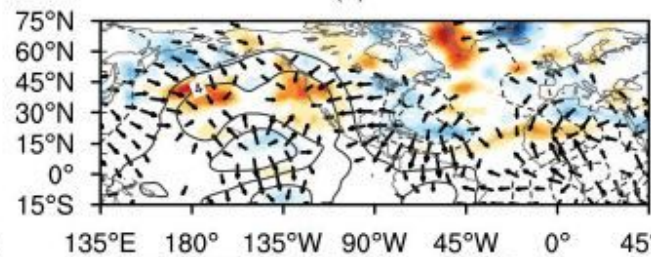
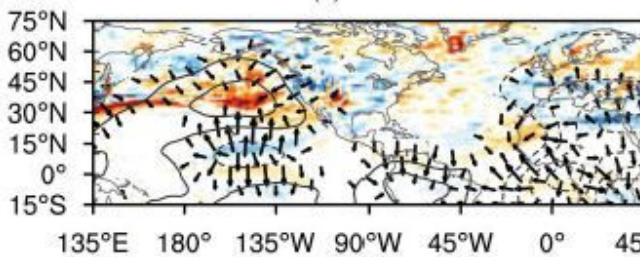
(b) IFS



(c)-(d) 250-hPa vp (contour), div wind (vector) and RWS (shading)

(c) CAM4

(d) IFS



(e)-(f) 250-hPa eddy Z (contour), WAF (vector) and RWS (shading)

(e) CAM4

(f) IFS

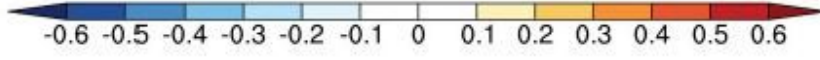
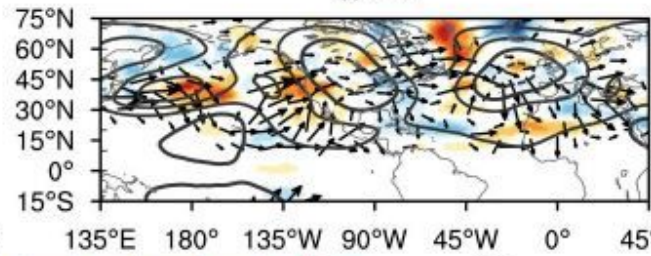
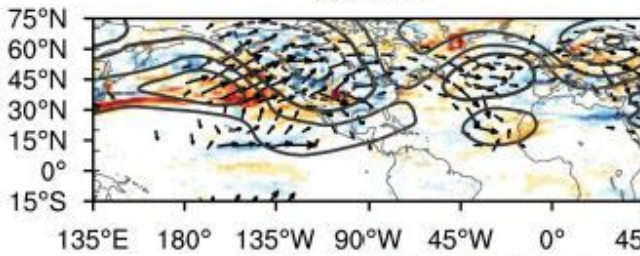
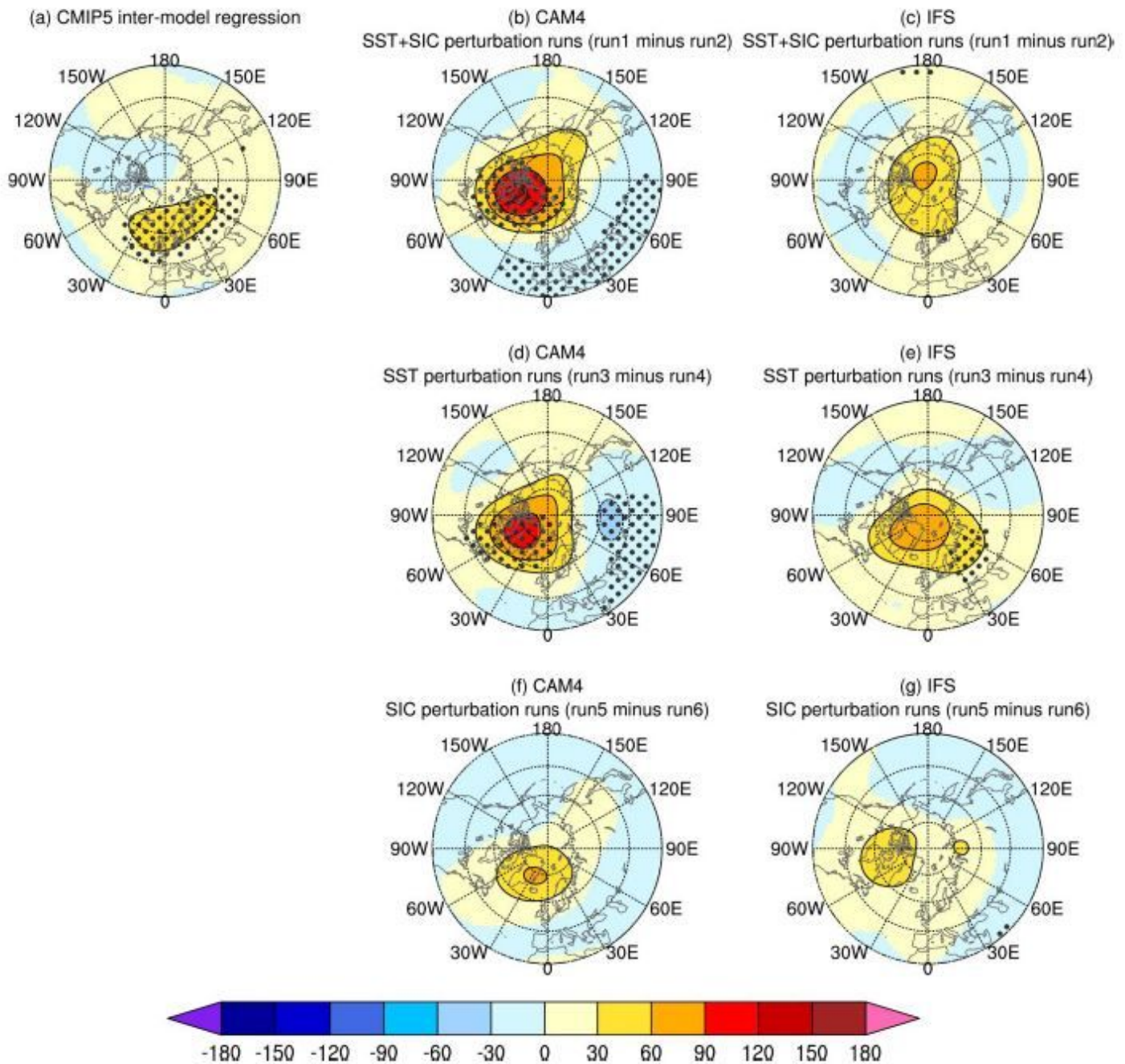


Figure 11

As in Fig. 6, but for the response in the SST perturbation runs: (left) CAM4 and (right) IFS. Note: The designations employed and the presentation of the material on this map do not imply the expression of any opinion whatsoever on the part of Research Square concerning the legal status of any country, territory, city or area or of its authorities, or concerning the delimitation of its frontiers or boundaries. This map has been provided by the authors.



**Figure 12**

Assessing the uncertainty in the DJF response of the 10-hPa geopotential height 927 (contour interval: 30 m) associated with PAΔSLP. (a) Inter-model regression of the forced 928 response against PAΔSLP across the ten CMIP5 models. The response of (middle) CAM4 and 929 (right) IFS in (b)–(c) the SST+SIC perturbation runs (run1 minus run2), (d)–(e) the SST 930 perturbation runs (run3 minus run4), and (f)–(g) the SIC perturbation runs (run 5 minus run6). 931 Unit: hPa. Shading indicates the 90% confidence level in the CMIP5 inter-model regression, 932 and the 95% confidence level in AGCM experiments based on the two-tailed Student's t-test. Note: The designations employed and the presentation of the material on this map do not imply the expression of any opinion whatsoever on the part of Research Square concerning

the legal status of any country, territory, city or area or of its authorities, or concerning the delimitation of its frontiers or boundaries. This map has been provided by the authors.

## Supplementary Files

This is a list of supplementary files associated with this preprint. Click to download.

- [SupplementaryCDV202103.pdf](#)